Electronic Supplementary Material (ESI) for Soft Matter.

Supporting Information

Fluid-solid transitions in photonic crystals of soft, thermoresponsive microgels

M. Hildebrandt,[1] D. Pham Thuy,[1] J. Kippenberger,[1] T. L. Wigger,[1] J. E. Houston,[2] A. Scotti,[3] and M. Karg[1]*

[1]Institut für Physikalische Chemie I: Kolloide und Nanooptik, Heinrich-Heine-Universität Düsseldorf, Universitätsstraße 1, D-40225 Düsseldorf, Germany

E-Mail: karg@hhu.de

[2]European Spallation Source ERIC, Box 176, SE-221 00 Lund, Sweden

[3]Institute of Physical Chemistry, RWTH Aachen University, Landoltweg 2, 52056 Aachen, Germany

List of samples

Core-shell (CS) microgel dispersions were prepared with various mass contents and filled into different capillaries depending on the type of measurements. Detailed information about the sample composition and the used capillaries are listed in **Table 1**. In order to maintain comparability between the samples prepared in H_2O and D_2O we used the same volume of solvent for dispersions made with the same mass of CS microgels. Thus, the dispersions possess the same particle number concentration in H_2O and D_2O. As an example, the 10.9 wt% sample prepared in D_2O and the 12 wt% sample prepared in H_2O have the same particle number concentration.

Table 1. List of the CS microgel dispersions prepared for the different experiments.

Mass content [wt%]	Dispersant	Capillary	Experiment
0.45	D_2O	rectangular	SAXS (20 °C)
5.4	D_2O	rectangular	SAXS (20 °C) / absorbance (various *T*)
7.3	D_2O	rectangular	SAXS (20 °C) / absorbance (various *T*)
9.1	D_2O	rectangular	SAXS (20 °C) / absorbance (various *T*)
10.9	D_2O	rectangular	SAXS (20 °C) / absorbance (various *T*)

1.25	H_2O	round	SAXS (40 °C)
5.4	D_2O	round	SAXS (40 °C)
7.3	D_2O	round	SAXS (40 °C)
9.1	D_2O	round	SAXS (40 °C)
12	H_2O	round	SAXS (40 °C)
10	H_2O	round	SAXS (determination of *N*)

Form factor analysis

We measured SAXS from dilute and concentrated core-shell (CS) microgel dispersions and radially averaged the scattering data to obtain the scattering intensity *I*, as function of the magnitude of the scattering vector *q*.

$$|\vec{q}| = q = \frac{4\pi}{\lambda} sin\frac{\theta}{2} \quad \text{(S1)}$$

The scattering angle is given by θ and λ is the wavelength of the X-rays.

In general, for the investigated *q*-range, the scattering intensity *I*(*q*), possessing the unit m^{-1} if measured in absolute units, can be described by the following equation:

$$I(q) = N{V_{\text{particle}}}^2 \Delta SLD^2 P(q) S(q) + I_{\text{B}} \quad \text{(S2)}$$

With *N* [m^{-3}] corresponding to the particle number density, V_{particle} [m^3] the volume of the scattering object and ΔSLD [m^{-2}] the difference in scattering length density (*SLD*) between the scattering object and the respective solvent. *P*(*q*) is the form factor of the scattering object, *S*(*q*) is the structure factor and I_B [m^{-1}] describes additional incoherent background contributions. For dilute dispersions, the structure factor can be neglected as $S(q) \approx 1$.

We note that here, the contrast of the investigated samples using SAXS is defined by the *SLD*s of the respective materials and the applied wavelength of the X-rays. Despite *SLD* being a *q*-dependent physical quantity, it is a suitable and well accepted quantity to describe contrast situations in SAXS as we already demonstrated in our previous work[1] and done so elsewhere.[2, 3]

The form factor modeling was performed with the SasView software.[4]

To describe the form factor of our CS microgels, we used a CS model:[5]

$$I(q) = \frac{scale}{V_{\mathrm{particle}}}\left[3V_{core}SLD_{\mathrm{core}}k(qR_{\mathrm{core}}) + 3V_{particle}SLD_{\mathrm{shell}}k\left(qR_{\mathrm{particle}}\right) - 3V_{core}SLD_{\mathrm{shell}}k(qR_{\mathrm{core}}) - 3V_{\mathrm{particle}}SLD_{\mathrm{solvent}}k\left(qR_{\mathrm{particle}}\right)\right]^2 + I_{\mathrm{B}} \quad \text{(S3)}$$

with

$$k(qR) = \frac{\sin(qR) - qR\cos(qR)}{(qR)^3}$$

With *scale* as scaling factor (corresponding to the volume fraction if measured in absolute units), *V* representing the volume of the respective scattering object and R_{core} and R_{particle} corresponding to the total radius of the core and the overall CS microgel. Here, R_{particle} is the sum of R_{core} and the thickness of the shell $\Delta t_{\mathrm{shell}}$. For the here probed *q*-range, the contrast is related to the *SLD*s of the respective materials. Due to their homogeneous and isotropic structure, the *SLD* of the solvent and the core is kept constant. *k*(*qR*) refers to the form factor oscillations of a spherical scattering object. In case of the CS microgels in their collapsed state, we used a constant *SLD* for the shell. For the CS microgels in their swollen state, we used an exponential decay in the *SLD* profile of the shell.

The exponentially decay in the scattering length density of the shell is described by:

$$SLD_{\mathrm{shell}}(R) = B\ exp\left(\frac{-A(R - R_{\mathrm{core}})}{\Delta t_{\mathrm{shell}}}\right) + C \quad \text{(S4)}$$

With $\Delta t_{\mathrm{shell}}$ being the thickness of the shell, and *A* being the decay constant. *B* and *C* are defined as:

$$B = \frac{SLD_{\mathrm{out}} - SLD_{\mathrm{in}}}{e^A - 1} \quad \text{(S5)}$$

$$C = \frac{SLD_{\mathrm{in}}e^A - SLD_{\mathrm{out}}}{e^A - 1} \quad \text{(S6)}$$

Here, SLD_{in} and SLD_{out} are the *SLD*s at $R_{\mathrm{in}} = R_{\mathrm{core}}$ and $R_{\mathrm{out}} = R_{\mathrm{particle}}$

The scattering length of the shell derived from the exponential *SLD* profile is given by:

$$f_{\mathrm{shell}} = 3\mathrm{BV}(R_{\mathrm{shell}})e^A h(\alpha_{\mathrm{out}}, \beta_{\mathrm{out}}) - 3BV(R_{\mathrm{core}})h(\alpha_{\mathrm{in}}, \beta_{\mathrm{in}}) + 3CV(R_{\mathrm{shell}})\frac{\sin(qR_{\mathrm{shell}}) - qR_{\mathrm{shell}}\cos(qR_{\mathrm{shell}})}{(qR_{\mathrm{shell}})^3} - 3CV(R_{\mathrm{core}})\frac{\sin(qR_{\mathrm{core}}) - qR_{\mathrm{core}}\cos(qR_{\mathrm{core}})}{(qR_{\mathrm{core}})^3} \quad \text{(S7)}$$

where

$$\alpha_{\mathrm{in}} = A\frac{R_{\mathrm{core}}}{\Delta t_{\mathrm{shell}}} \tag{S8}$$

$$\alpha_{\mathrm{out}} = A\frac{R_{\mathrm{shell}}}{\Delta t_{\mathrm{shell}}} \tag{S9}$$

$$\beta_{\mathrm{in}} = qR_{\mathrm{core}} \tag{S10}$$

$$\beta_{\mathrm{out}} = qR_{\mathrm{shell}} \tag{S11}$$

and

$$h(x,y) = \frac{x\sin(y) - y\cos(y)}{(x^2+y^2)y} - \frac{(x^2-y^2)\sin(y) - 2xy\cos(y)}{(x^2+y^2)^2 y} \tag{S12}$$

The polydispersity of the core and the shell of our CS microgels are included using a Gaussian distribution of the respective radii. Here, $\langle r \rangle$ is related to the average particle radius, and σ_{poly} describes the relative size polydispersity.

$$D\left(R, \langle R\rangle, \sigma_{\mathrm{poly}}\right) = \frac{1}{\sqrt{2\pi{\sigma_{\mathrm{poly}}}^2}} exp\left(-\frac{(R-\langle R\rangle)^2}{2{\sigma_{\mathrm{poly}}}^2}\right) \tag{S13}$$

Due to the distinct difference in core and shell size, we can also fit the core contribution only. To describe the scattering intensity of the silica cores, we applied a simple polydisperse sphere model:

$$I(q) = \frac{scale}{V_{\mathrm{particle}}}\left[3V(R)\Delta SLD\,\frac{\sin(qR) - qR\cos(qR)}{(qR)^3}\right]^2 + I_{\mathrm{B}} \tag{S14}$$

The parameters used for the fits are listed in **Table S2**.

Table S2. Parameters applied to fit the scattering profiles of the dilute CS microgel dispersions in their swollen (T = 20 °C) and collapsed state (T = 40 °C).

Parameters	Core-exponential-shell (swollen state)	Core-homogeneous-shell (collapsed state)
scale	0.029	2.733
I_B [a. u.]	0.2	0.003
R_{core} [nm]	18	18
Δt_{shell} [nm]	120	72
SLD_{core} [10^{-6} Å^{-2}]	17.75	17.75
$SLD_{shell,\ in}$ [10^{-6} Å^{-2}]	9.89	10.30
$SLD_{shell,\ out}$ [10^{-6} Å^{-2}]	9.43	-
$SLD_{solvent}$ [10^{-6} Å^{-2}]	9.43	9.43
σ_{core}	0.1	0.1
σ_{shell}	0.1	0.08
A	2.2	-

We began the fitting procedure using fixed values for the background (I_B), R_{core}, σ_{core}, $SLD_{solvent}$, and SLD_{core}. Prior to the first fitting-steps, reasonable values for the Δt_{shell}, SLD_{shell} and σ_{shell} were assumed to get a starting point for the fitting-procedure. Next, the parameters were fitted in the following order: *scale*, SLD_{shell}, Δt_{shell}, *A* (decay constant), σ_{shell}. The values obtained from each fitting-step were applied for the following step. In each step, only the respective parameter was set free to change, while the other parameters were kept constant. As the model consists of many parameters, setting all parameters free resulted in a fit no longer describing the data sufficiently well when using SasView. Therefore, the procedure was repeated until the fit described the experimental data sufficiently well.

Prior to the synchrotron SAXS experiments, R_{core} and σ_{core} were determined from inhouse SAXS measurements presented in **Figure S13**. The q-range in the experiment was limited in the high-*q* regime and we were only able to fit the scattering of the core. Due to this, the values were already known and could kept constant in the fitting-procedure regarding the CS microgels.

We also applied other form factor models including the core-shell microgel model that is based on the widely accepted fuzzy-sphere model to describe the inhomogeneous

morphology of microgel shell.[6, 7] **Figure S1** compares the results for a simple CS model (homogeneous shell) in orange, the core-shell microgel model that is described by a box like profile for the core and the inner homogeneous region of the microgel shell with respective constant *SLD*s followed by an error function like decay similar to the fuzzy sphere model in green[7] and the previously discussed CS model with exponentially decaying shell in red. These additional form factor fits were performed with the SASfit software.[8]

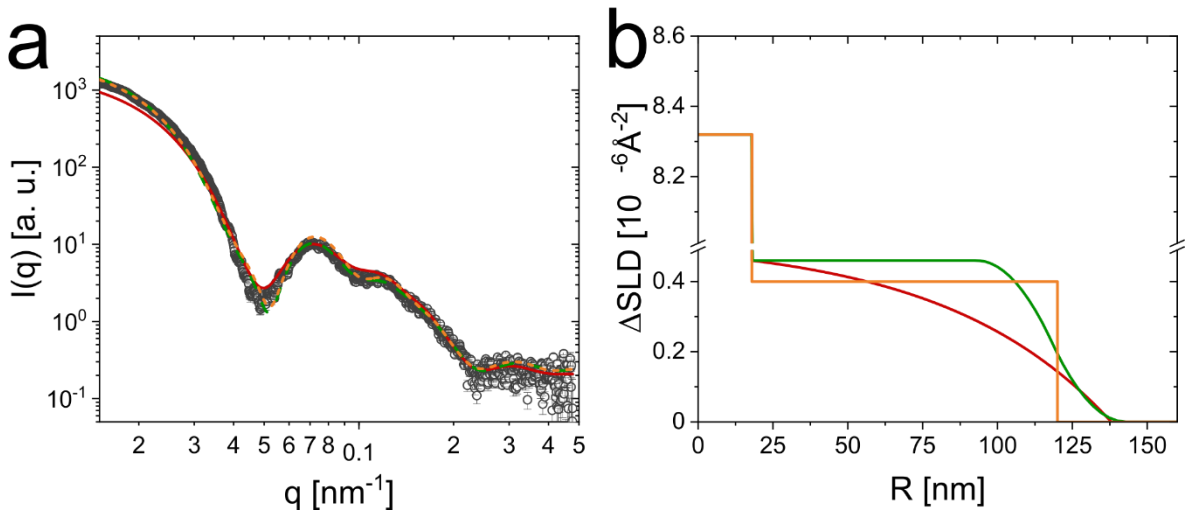

Figure S1: Comparison of different form factor models. (a) SAXS profile recorded from a dilute CS microgel dispersion with solid lines corresponding to fits using a core-shell model with an exponentially decay in the *SLD* of the shell (red, **eq. S3** and **eq. S4**), the core-shell microgel model[7] (green, dashed line) and a core-shell model with homogeneous *SLD* profiles for the core and the shell (orange, dashed line). (b) Radial profiles of the difference in *SLD*s, based on the shown form factor fits with the same color coding as in (**a**).

Figure S1a shows that all three applied CS models can describe the SAXS profile of our CS microgels quite well. Deviations occur in the low and mid *q*-range where the shell scattering dominates. The parameters used to fit the scattering intensities are listed in **Table S3**. The radial density profiles extracted from the respective CS models are shown in **Figure S1b**. All models exhibit a high *ΔSLD* value related to the core until a radius of 18 nm. From this point on, we can see an exponential decay for the core-exponential-shell model (red) and a constant *ΔSLD* for the core-shell model (orange). The core-shell microgel model (green) exhibits the box like profile with a constant *ΔSLD* followed by a decay ascribed to the fuzzy surface of a microgel.[7] The core-exponential-shell and the core-shell microgel model result in similar total radii of 138 ±

14 nm and 143 ± 27 nm, while the core-shell model yields a much smaller radius with just 120 nm. Despite the fact that the simple CS model with homogeneous *SLD* profiles for core and shell describes the experimental data very well, we do not further consider this model because the homogeneous density profile of the shell is rather unrealistic given the known crosslinker gradient towards the periphery of the microgel shell.[9] In order to obtain reasonable fits with the core-shell microgel model, a polydispersity as large as 20% was imposed on the homogeneous box profile, which is very unrealistic according to our results from dynamic light scattering, where the polydispersity was below 10%. Therefore, despite the good description of the experimental data with this model, we decided to not further consider this rather complex form factor model with a large number of fits parameters. We conclude that the core-exponential-shell model leads to more realistic results for the size, morphology and polydispersity of the CS microgels. Furthermore, due to the lower number of possible fit parameters, we decided to use the core-exponential-shell model in the following of this work.

Table S3. Fit parameters obtained from different form factor models.

Parameters	**Core-exp.-shell[5]**	**Core-shell microgel[7]**	**Core-shell**
R_{core} [nm]	18	18	18
[1]Δt_{shell} [nm]	120	75	102
[2]$sigma_{out}$ [nm]	-	25	-
[3]SLD_{core} [10^{-6} Å^{-2}]	17.75	17.75	17.75
[3]SLD_{shell} [10^{-6} Å^{-2}]	9.89	9.89	9.83
[3]$SLD_{solvent}$ [10^{-6} Å^{-2}]	9.43	9.43	9.43
[3]σ_{core}	0.1	0	0
σ_{shell}	0.1	0.2	0.15
[2]A	2.2	-	-

[1] According to the SASfit manual Δt_{shell} is given as W_shell and SLD_X refers to eta$_X$ being the scattering length density of the respective material. Parameters corresponding to the core-shell microgel model according to the SASfit manual not being listed here are set to zero.

[2] Parameters without any given value are not present in the respective model.

[3] In SASfit polydispersity can only be applied on one parameter, therefore we choose the thickness of the shell (Δt_{shell}) being the more relevant quantity in this case.

Dynamic light scattering

In addition to the temperature dependent DLS measurements shown in **Figure S2a**, we performed angle-dependent DLS measurements below and above the volume phase transition temperature (VPTT) at 20°C and 45°C, respectively. The decay

constants, Γ, were computed from the normalized field-time autocorrelation functions using the CONTIN algorithm[10] via the AfterALV software (v1.06d, Dullware, Amsterdam, The Netherlands).

Plotting the values of Γ against q^2 (**Figure S2b**) we can extract the translational diffusion coefficient, D_T, with high precision:

$$D_T = \frac{\bar{\Gamma}}{q^2} \tag{S15}$$

The Stokes-Einstein equation can then be applied to determine the hydrodynamic radius R_h:

$$D_T = \frac{kT}{6\pi\eta R_h} \tag{S16}$$

Here, k is the Boltzmann constant, T is the absolute temperature and η is the viscosity of the solvent.

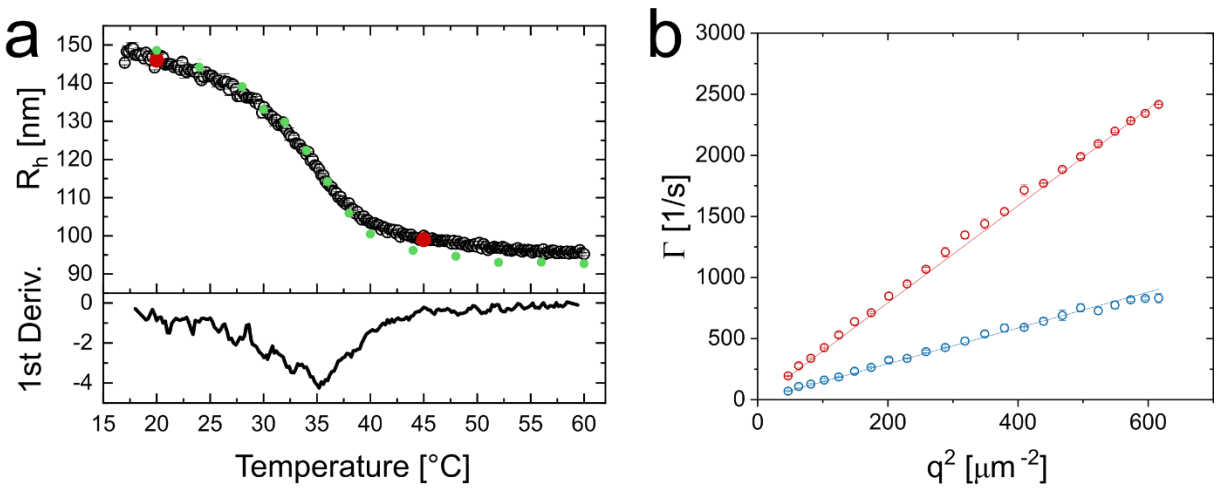

Figure S2. (a) Hydrodynamic radius as function of temperature obtained from fixed angle measurements in H_2O (black circles, Zetasizer), D_2O (green circles, Zetasizer) and angle-dependent DLS (red circles, H_2O). (b) Decay constants from angle-dependent DLS as function of q^2. The blue circles correspond to the data recorded at 20 °C and the red circles were recorded at 45 °C. The straight lines correspond to linear fits to the data.

Translational diffusion coefficients of $1.47 \cdot 10^{-12}$ m^2/s and $3.97 \cdot 10^{-12}$ m^2/s were extracted from the linear fits and correspond to R_h of 146 ± 1 nm at 20°C and 99 ± 1 nm at 45 °C presented as red circles in **Figure S2a**. The obtained values form angle-dependent DLS match well to the results from the temperature dependent measurements with a R_h of 147 ± 3 nm at 20 °C and 100 ± 1 nm at 45 °C. In addition, we extracted a VPTT of 35.1 °C for the

CS microgels based on the 1st derivative of the temperature dependent DLS data. To investigate isotope effects on the thermoresponsive properties of the CS microgels we performed temperature dependent DLS measurements in D_2O as solvent. The R_h is shown as function of the temperature as green circles in **Figure S2a**. A deviation from the hydrodynamic radii recorded in H_2O is only visible for temperatures above 38 °C as the particles exhibit a R_h of 100 ± 1 nm in D_2O and 103 ± 1 nm in H_2O at a temperature of 40 °C. Up to the temperature of 38 °C, the hydrodynamic radius determined in H_2O describes the size of the CS microgels sufficiently well, independent of the here used solvents.

Figure S3 shows the electrophoretic mobility of the CS microgels in aqueous dispersion. At low temperatures, in the swollen state, the microgels possess rather small, negative values of mobility, until a temperature of 35 °C. Here, the mobility strongly decreases until reaching a constant value at about 55 °C. The decrease in mobility is associated to the reduction in size of the CS microgel when undergoing the VPT. Here, the surface area decreases and thus the effective charge density over the CS microgel increases. Please note that the CS microgel is negatively charged and an increase in charge per area is reflected by a decrease in electrophoretic mobility.

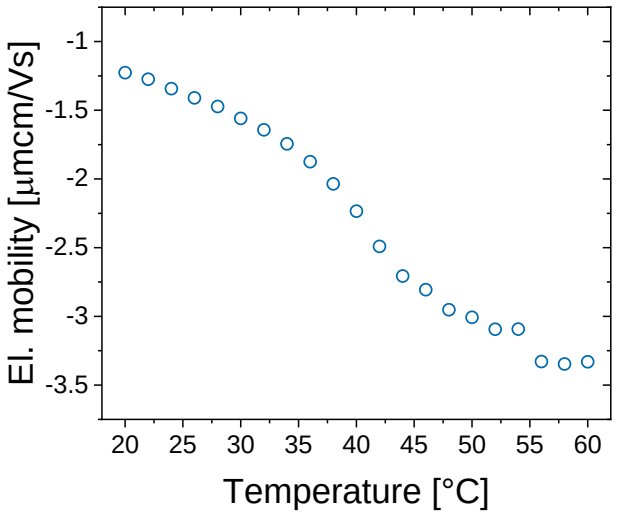

Figure S3. Electrophoretic mobility of the CS microgels in dilute, aqueous dispersion as function of temperature.

SAXS investigation of the silica cores

The scattering profile of the SiO_2 cores prior to the encapsulation in the PNIPAM shell is presented in **Figure S4** and shows multiple form factor oscillations between q = 0.15

– 1.0 nm^{-1}. We fitted the scattering data with a homogeneous sphere model (red solid line) yielding a radius of 18 ± 2 nm with a polydispersity of 10%.

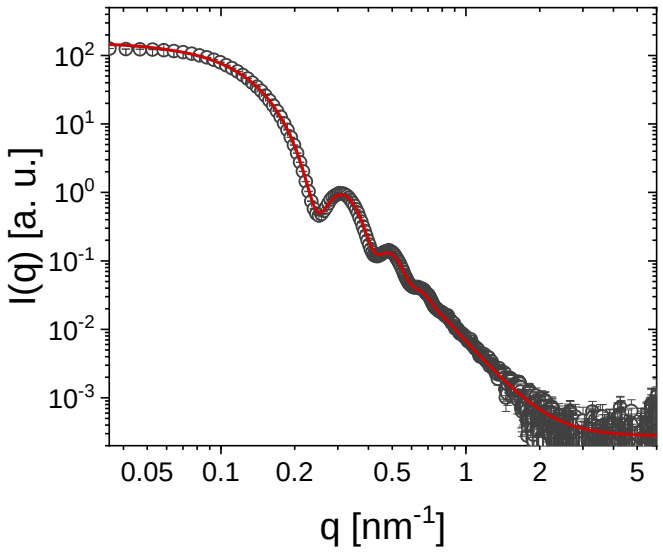

Figure S4. Scattering profile of the SiO_2 cores prior to the encapsulation in PNIPAM shells. The solid line is related to a hard sphere form factor fit (**eq. S14**).

Transmission electron microscopy investigation

The successful encapsulation of the silica cores and general morphology of the CS microgels was investigated with transmission electron microscopy (TEM). We used the images shown in **Figure S5a-c** to determine the encapsulation rate of the SiO_2 nanoparticles (NPs), the average core size and its size distribution which is presented in **Figure S5d**. The histogram is based on manual image analysis using the image analysis software imageJ.[11] The size distribution can be described with a Gaussian distribution function resulting in an average radius of 18 ± 2 nm.

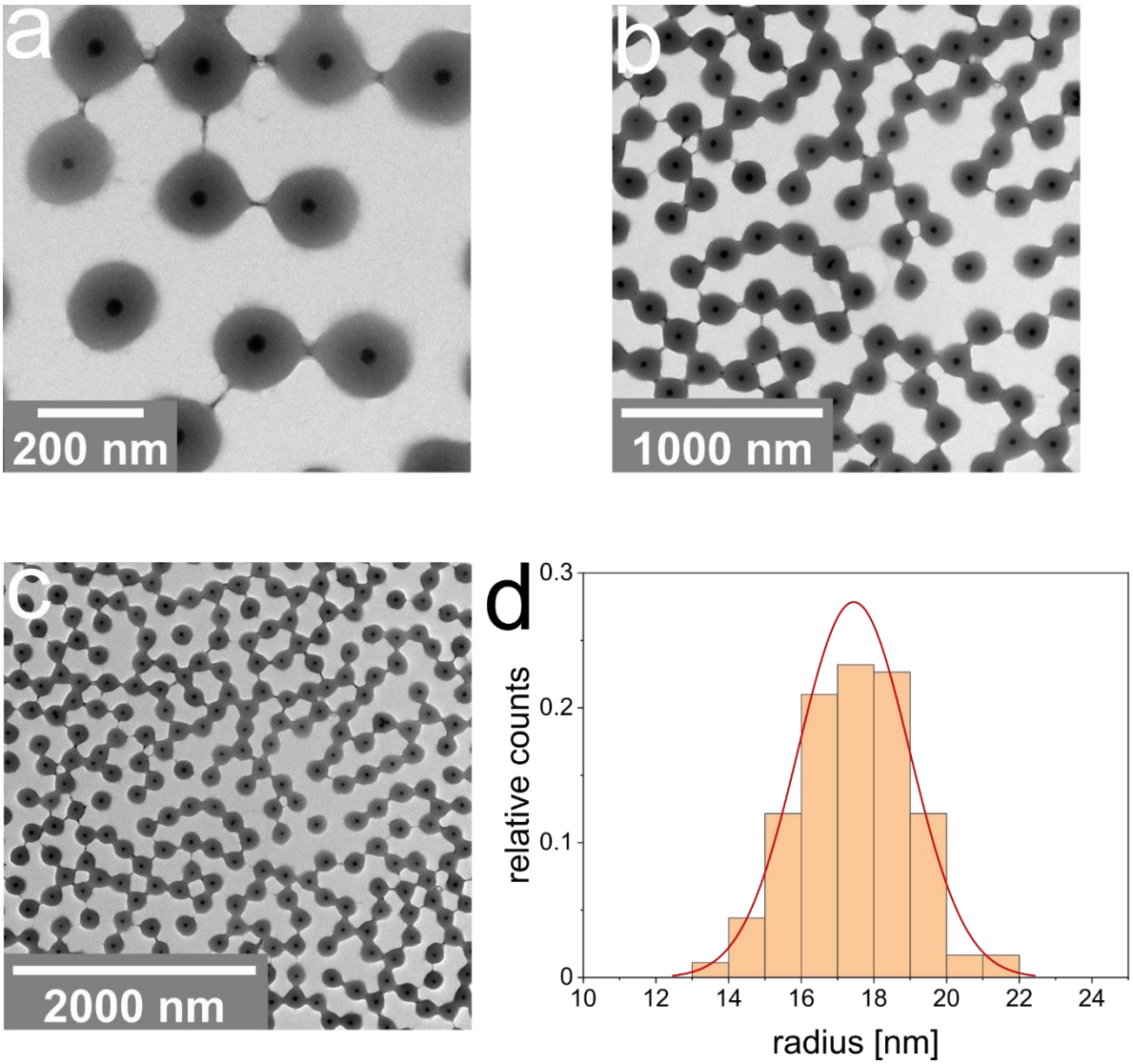

Figure S5. Representative TEM images of the CS microgels at different magnifications (a-c) and a histogram related to the size distribution of the SiO_2 cores with a fit to the data using a Gaussian distribution function (red line) (d).

Sample annealing

After sample preparation at room temperature, we performed a detailed annealing procedure where the temperature is increased from 20 °C to 50°C with a rate of 1.5 K/h using a high precision circulating water bath. At 50 °C the temperature is kept constant for one hour and is then again lowered to 20°C with a cooling rate of 1.5 K/h. The time dependent evolution of the temperature is shown in **Figure S6**.

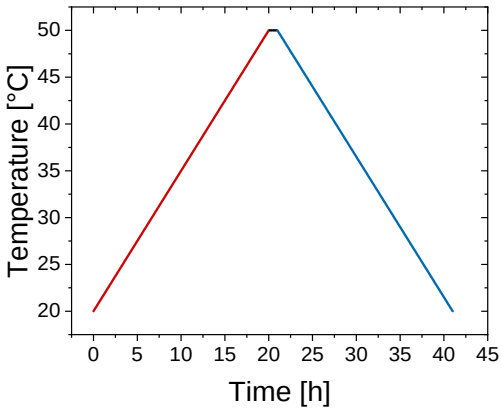

Figure S6. Temperature profile used for sample annealing.

Vis-NIR absorbance spectra from different points in time

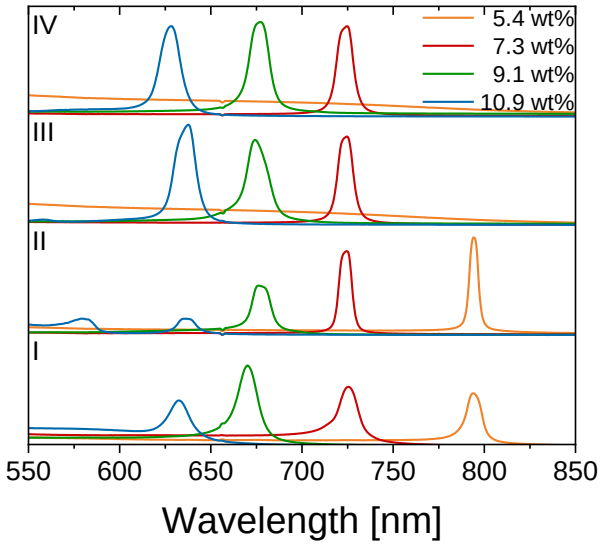

Figure S7. Vis-NIR absorbance spectra recorded at different points in time. From the bottom to the top: Directly after sample preparation (I), after annealing (II), half a year after sample preparation (III) and directly after SAXS measurements (IV).

Vis-NIR absorbance spectra were recorded at different points in time at 20°C, to verify the stability of the colloidal crystals (CC). The spectra at the bottom of **Figure S7** (I) were recorded directly after sample preparation and show Bragg peaks for all samples. After the annealing procedure (II) the spectra exhibit sharper Bragg peaks for the 5.4 and 7.3 wt% samples indicating an increased crystallinity. The samples with 9.1 and 10.9 wt% show a decrease in the intensity of the Bragg peak. We attribute this to the

absence of large crystalline domains in the monitored sample volume. We note that the samples were measured in specific sample holders which do not allow for any changes in the position of the capillary. Afterwards samples were directly stored at 4°C. The next series of absorbance spectra (III) was recorded half a year after sample preparation and all samples excluding the 5.4 wt% exhibit distinct Bragg peaks. We conclude that the 5.4 wt% sample does not show stable colloidal crystals in long time equilibrium state. The improvement in the Bragg peak quality, in the observed volume, might be attributed to a temperature change of the samples during the transfer of the samples to a different location. Here, some rearrangements within the sample might occur resulting in higher quality Bragg peaks in the probed volume. Spectra recorded after the SAXS measurements (IV) show similar appearance compared to (III). A distinctive change in the Bragg peak position of the CS microgel dispersions is not detectable over the complete series of measurements.

Crystal analysis by Vis-NIR and angle-dependent specular reflectance spectroscopy

We measured concentrated dispersions of CS microgels that exhibit distinct and narrow Bragg peaks at wavelengths, λ_{Bragg}, that are related to the respective diffraction order m, the incident angle θ and the spacing between the respective lattice planes d_{hkl}. Theoretically, the Bragg peak position is described by a combination of Snell's law and Bragg's law:[12]

$$m\lambda_{\mathrm{diff}} = 2\, d_{\mathrm{hkl}} \sqrt{{n_{\mathrm{crystal}}}^2 - \sin\theta^2} \qquad \text{(S16)}$$

We used an average refractive index for the CS microgel dispersion of $n_{crystal}$ = 1.345 as reported in literature for a similar system.[13]

Exemplary angle-dependent specular reflectance spectroscopy measurements were conducted with the 9.1 wt% sample. In **Figure S8** we show the relation between the angle of the incident beam and the position of the Bragg peak. The black vertical lines indicate the theoretically expected Bragg peak positions for a d_{hkl} = 251 nm. An absorbance spectrum recorded in transmission geometry to represent the Bragg peak position at an angle of 0° is shown in red. We see a distinct blue shift of the Bragg peak

with an increase in the respective angle. The experimental data and the theoretical peak positions are in good agreement.

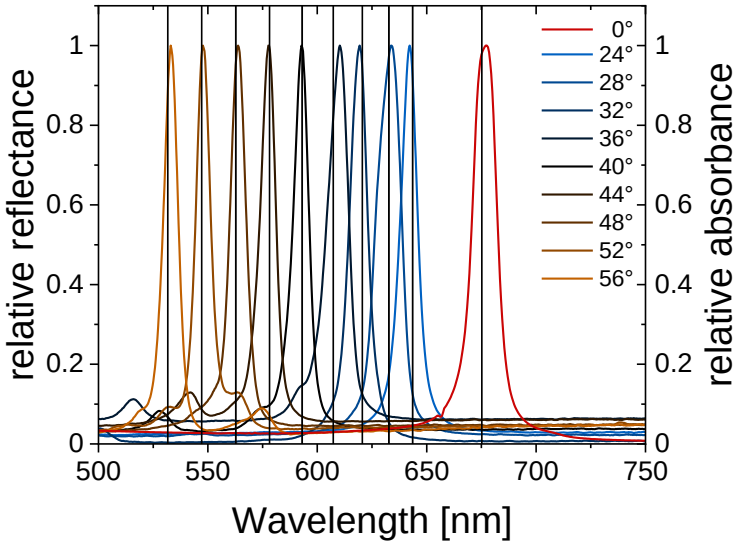

Figure S8. Normalized angle-dependent specular reflectance measured form the 9.1 wt% sample. The red spectrum is related to an absorbance measurement in transmission geometry (0 °). Black vertical lines indicate the theoretical peak positions based on a hcp lattice.

When the samples are measured in transmission geometry and θ corresponds to the angle between the optical normal and the incident beam $\theta = 0°$ leading to:

$$\lambda_{\mathrm{Bragg}} = 2\, d_{\mathrm{hkl}}\, n_{\mathrm{crystal}} \tag{S17}$$

Assuming a hexagonal closed packed (hcp) crystal structure the spacing between lattice planes, d_{hkl} is connected to the lattice parameters *a* and *c* by:

$$d_{hkl} = \frac{a}{\sqrt{\frac{4}{3}(h^2+hk+k^2)+\frac{a^2}{c^2}l^2}} \tag{S18}$$

Here, *h*, *k* and *l* correspond to the Miller indices. In case of a closed packed lattice of isotropic spheres the ratio between *c* and *a* is fixed to a value of $(8/3)^{1/2}$. This is due to the geometry of the unit cell at dense packing of spheres with a volume fraction of 0.74. With the known ratio we can rewrite **equation S18** to yield the lattice constant *a*:

$$a = d_{hkl}\sqrt{\frac{4}{3}(h^2+hk+k^2)+\frac{3}{8}l^2} \tag{S19}$$

With the **equations S17** and **S19,** we can extract the lattice constant *a* from the position of the Bragg peak in the Vis-NIR absorbance spectrum.

$$a = \frac{\lambda_{\mathrm{diff}} \sqrt{\frac{4}{3}(h^2+hk+k^2)+\frac{3}{8}l^2}}{2\, n_{\mathrm{crystal}}} \tag{S20}$$

When we assign the 002 plane to the Bragg peak, we can write **equation S20** in the following way:

$$a = \frac{\lambda_{\mathrm{diff}} \sqrt{\frac{3}{2}}}{2\, n_{\mathrm{crystal}}} \tag{S21}$$

The volume fraction ϕ of an hcp crystal with 3 + 3 spheres contributing to one unit cell can be calculated with the lattice constant *a* and the radius *R* of the spheres.

$$\phi = \frac{(3+3)\frac{4}{3}\pi R^3}{\frac{3\sqrt{3}\sqrt{\frac{8}{3}}a^3}{2}} \tag{S22}$$

Temperature dependent Vis-NIR absorbance spectroscopy

We performed temperature dependent Vis-NIR spectroscopy with crystalline CS microgel dispersions which exhibit Bragg peaks. The spectra were recorded between 20 °C and 50 °C in steps of 0.3 °C. The samples were equilibrated for twelve minutes before each measurement. Due to the slow heating and cooling rates, we can assume that the sample is close to equilibrium conditions during the whole procedure. This is illustrated in **Figure S9a**, while in **Figure S9b** a small section of the procedure is shown to clarify the stepwise approach. We note that **Figure S9** excludes the time needed for the sample holder to change temperature, and the time for conducting the measurement itself.

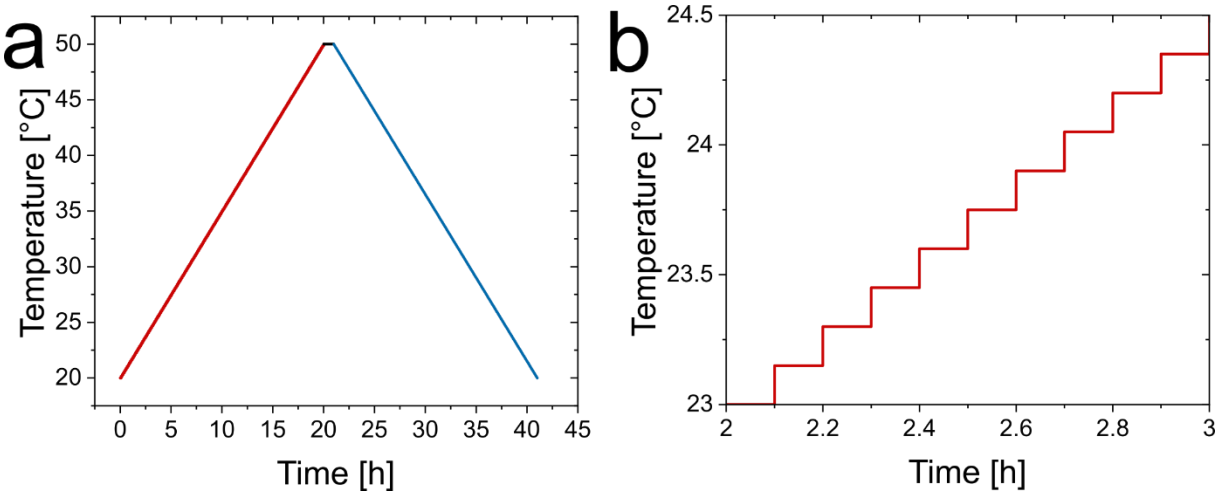

Figure S9. Temperature profiles used for Vis-NIR absorbance measurements. (a) Time dependent evolution of the temperature and a small section (b) showing the stepwise increase of the temperature.

The temperature dependent Vis-NIR spectra are shown in **Figure S10** and were recorded between 20 °C and 50 °C in 0.3 °C steps indicated by the color transition from dark blue (20 °C) to red (50 °C). The four rows correspond to the mass contents of 7.3 wt% (a), 9.1 wt% (b, c) and 10.9 wt% (d) CS microgel dispersions. Noteworthy, for 9.1 wt% an additional sample was measured to verify the reproducibility of the measurements. For each sample, we observe a decrease in the absorbance of the Bragg peak in a certain temperature range, which is visible in the absorbance spectra and marked in green for the respective plots of the Bragg absorbance as function of the temperature. In this temperature range, the sample undergoes the phase transition from a crystalline to a disordered system. Based on the conducted experiment, we can extract the transition temperature of the respective CS microgel dispersion (**Table S4**). This is done by applying linear fits on the green colored transition section were the Absorbance of the Bragg peak decreases and the blue colored section where the Bragg peak absorbance is 0. The intercept of both fits on the x-axis is listed as transition temperature.

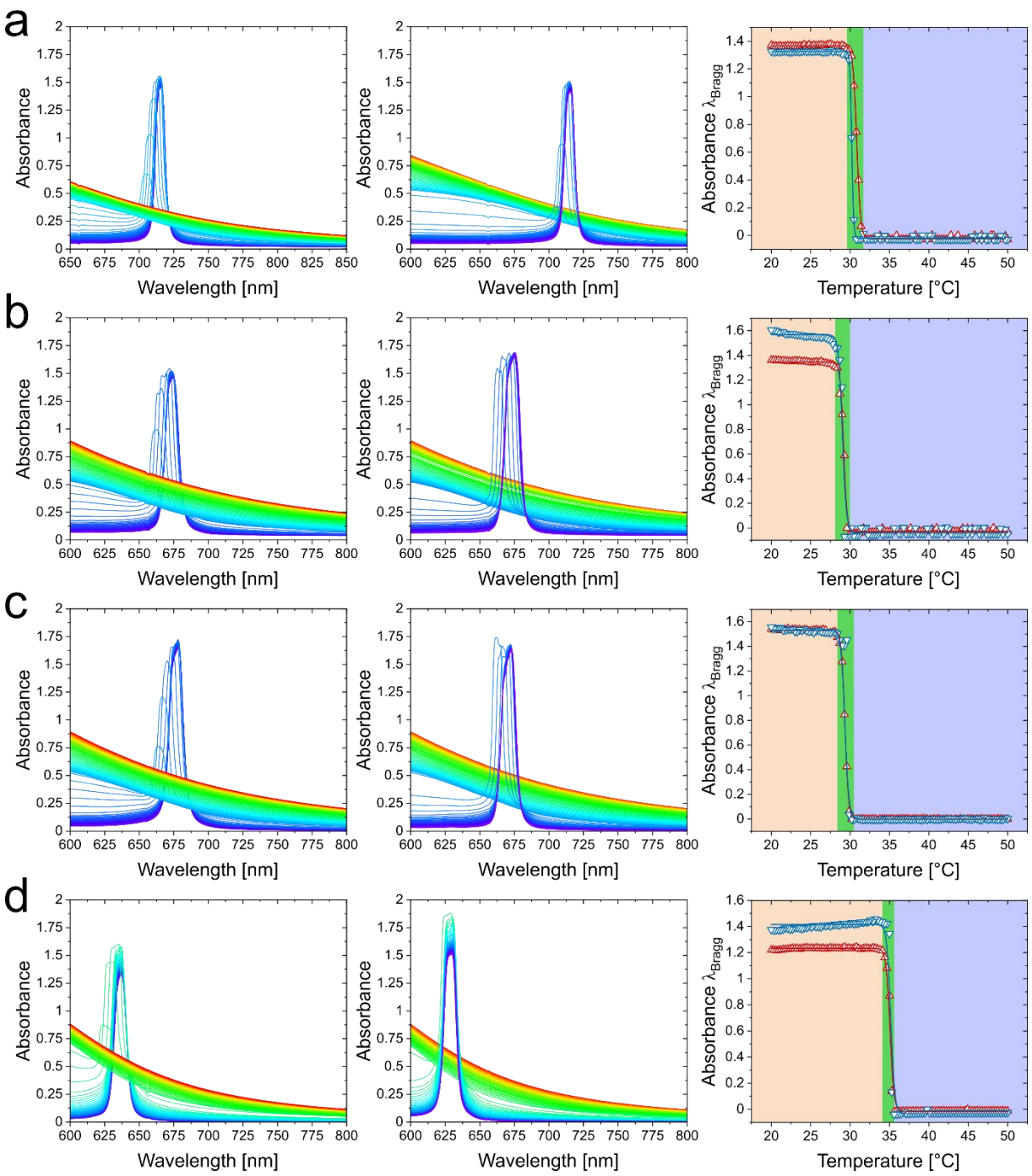

Figure S10. Temperature dependent Vis-NIR absorbance spectra and the respective Bragg peak intensity as function of the temperature from 7.3 wt% (a), 9.1 wt% (b, c) and 10.9 wt% CS microgel dispersion. The spectra in the left row correspond to a heating cycle while the spectra in the middle column correspond to a cooling cycle. Spectra were recorded from 20°C to 50°C and vice versa with 0.3°C steps indicated by the color transition from blue to red.

Table S4. Transition temperatures of the respective CS samples.

Mass content [wt%]	$T_{transition}$ (heating) [°C]	$T_{transition}$ (cooling) [°C]
7.3	31.6	30.7
9.1	29.8	29.9
9.1	30.2	30.3
10.9	35.7	35.5

Figure S11a shows the time-dependent evolution of the Bragg peak at fixed temperatures. In **Figure S11b**, the absorbance of the Bragg peak at fixed temperatures is plotted as function of time. It is clearly visible that the Bragg peak decreases within the first 100 seconds and remains at a constant value for the rest of the observed time window (a total time of 1800 s). This implies that for the performed temperature-dependent Vis-NIR spectroscopy measurements, with equilibration time of 720 s between each temperature step, the CS microgel dispersion has reached its equilibrium state.

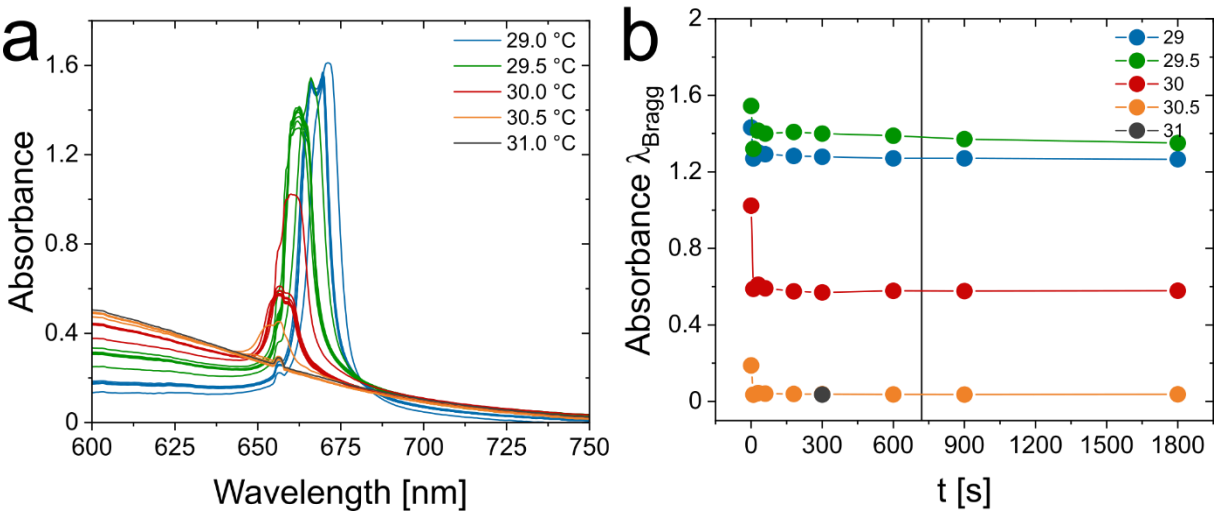

Figure S11. Time-dependent evolution of the Bragg peak at fixed temperatures recorded from a 9.4 wt% CS microgel dispersion. (**a**) Time-dependent Vis-NIR absorbance spectra recorded at fixed temperatures after a prior, fast temperature increase by 0.5 K. (**b**) Time-dependent evolution of the Bragg peak absorbance.

Density of the silica cores

In order to extract the number concentration from SAXS profiles the density of the scattering objects is required. In our case, the form factor of the core is used for the

analysis and thus the density of the silica cores was determined. To do so, the dispersion of silica cores was purified via dialysis against ultra-pure water and the density of a series of dilute dispersions with various concentrations was measured. From a plot of the reciprocal density of the respective dispersions against the respective mass content, the density of the SiO_2 NPs can be extracted with the following equation:

$$\rho = \frac{1}{w_f m + b} \implies \frac{1}{\rho} = w_f m + b \qquad \text{(S23)}$$

Here, ρ is the density of the dispersed particles, w_f being the mass fraction and m and b are related to the slope and the y-intercept of the linear fit as shown in **Figure S12,** where the reciprocal density of the dispersion is plotted as function of the silica mass fraction.

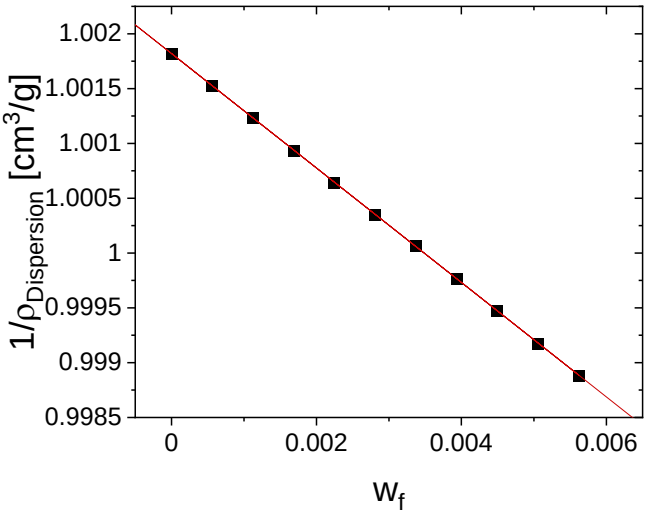

Figure S12. Reciprocal density of dilute SiO_2 NP dispersions against the mass content of the respective dispersion. The red line corresponds to the linear function used to fit the data.

The linear function describes the data very well and a slope of -0.52204 cm^3/g and a y-intercept of 1.00182 cm^3/g is obtained. According to equation S15 a density of 2.08 g/cm^3 for the SiO_2 NPs can be determined.

Extraction of number concentrations from SAXS

Additional SAXS measurements were performed with the intensity in absolute units on four (I-IV) concentrated CS microgel dispersions to determine the number concentrations based on the scattering contribution of the SiO_2 cores.[1, 9] A total number

of four samples with the same mass content were investigated to ensure that the performed measurements lead to representative results and to obtain a standard deviation regarding the number concentration. The SAXS profiles of the CS microgel dispersions (10 wt%, H_2O), including form factor fits (solid lines) are shown in **Figure S13**. The applied polydisperse sphere model describes the data sufficiently well in the respective *q*-range and the fit parameters are listed in **Table S5**. We see the first form factor minimum at approximately 0.2 nm^{-1} and discrepancies between the measured data and the form factor fit below q = 0.06 nm^{-1}. The deviation is related to scattering of the shell which is not described by the model used here. The data of the four different CS microgel dispersions superimpose each other, as well as the form factor fits. This is expected as all samples possess the same concentration. Even though 10 wt% is a concentration high enough that strong structure factor contributions will occur, our analysis is reasonable since we focus on the form factor of the cores that are much smaller than the total CS microgel dimensions. In other words, the structure factor from the lattice of CS microgels and the form factor of the small cores appear in different regimes of *q*. In particular the pronounced form factor oscillations visible in **Figure S13** are not affected by the structure factor. Therefore, we can use the analysis of relatively high and thus well strongly scattering samples to deduce the number concentration of cores and consequently the CS microgels based on the assumption that each CS microgel contains a single silica core. Consequently, the number concentration of the cores is the same as the number concentration of the CS microgels.

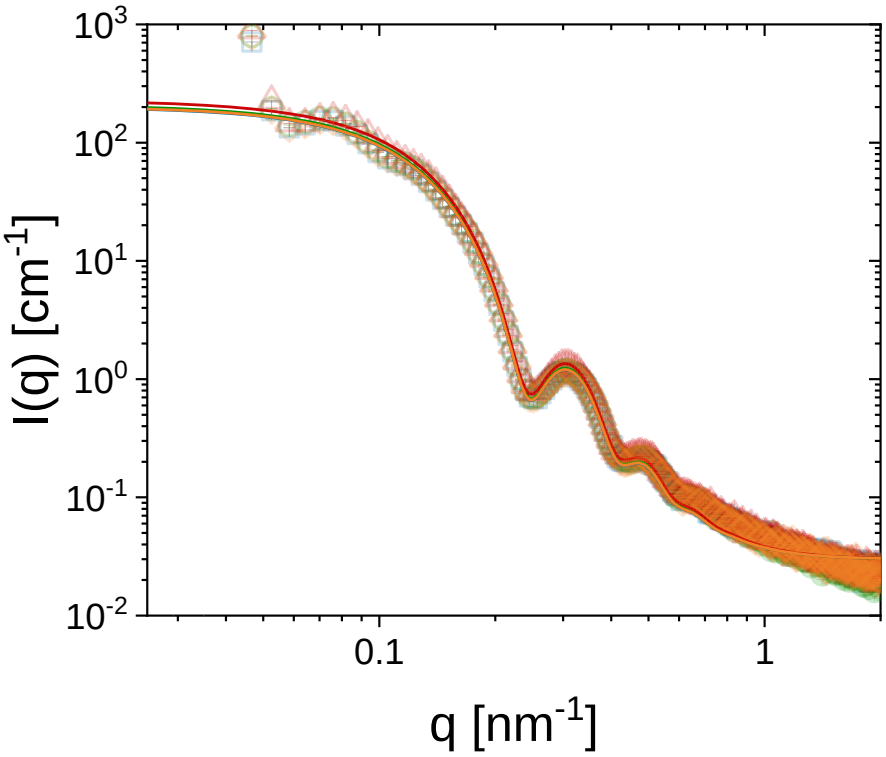

Figure S13. SAXS profiles of four different samples (each 10 wt% CS microgels) and the respective form factor fits (sphere-model, **eq. S14**) to the core scattering contribution (solid lines).

Table S5. Fit parameters obtained from the form factor fits. The Errors of the parameters are smaller by two orders of magnitudes compared to the obtained valuers and therefore not listed.

	I	II	III	IV
scale	0.00107	0.00108	0.00111	0.00121
I_B [cm^{-1}]	0.03	0.03	0.03	0.03
SLD (SiO_2) [10^{-6} $Å^{-2}$]	17.75	17.75	17.75	17.75
SLD (H_2O) [10^{-6} $Å^{-2}$]	9.47	9.47	9.47	9.47
R [nm]	18	18	18	18
σ_{poly}	0.1	0.1	0.1	0.1

In order to calculate the number concentration *N*, the scattering intensity at infinitely small *q*, I_0 needs to be known. Therefore, the SAXS data in absolute units are plotted in a Guinier plot, *i.e.* ln(*I*(*q*)) as function of q^2 according to:

$$\ln\big(I(q)\big) = \ln(I_0) - \frac{q^2 {R_G}^2}{3} \qquad \text{(S24)}$$

In addition to I_0, we can extract the radius of gyration R_G from a linear fit to the data. As presented in **Figure S14**, we performed the Guinier analysis not only on the scattering profile but also on the performed form factor fits of the core. This is due to the form factor oscillations of the shell, which occur for $q^2 < 0.015$ nm^{-2} and might influence the results of the Guinier analysis. To prevent possible corruption of the extracted I_0 due to the scattering of the shell we used the I_0 extracted from the Guinier analysis of the form factor fits of the core. The results from the Guinier analysis are presented in **Table S6** and **Table S7.**

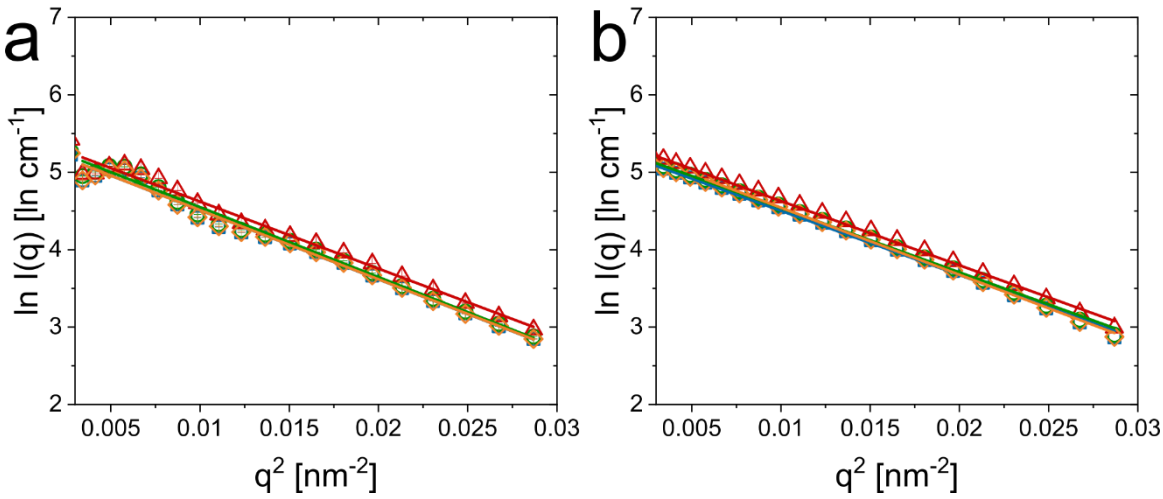

Figure S14. Guinier plots of the scattering data (a) and the respective form factor fits (b).

Table S6. Results from the linear fits applied on the Guinier plots of the SAXS data.

	I	II	III	IV
I_0 [cm^{-1}]	221 ± 10	233 ± 10	242 ± 10	221 ± 9
R_G [nm]	16.4 ± 0.3	16.5 ± 0.3	16.1 ± 0.3	4 ± 0.3

Table S7. Results from the linear fits applied on the Guinier plots of the form factor fits.

	I	II	III	IV
I_0 [cm^{-1}]	206 ± 2	215 ± 2	235 ± 2	224 ± 3
R_G [nm]	15.8 ± 0.1	15.8 ± 0.1	15.8 ± 0.1	16.2 ± 0.1

Both approaches give comparable results with a radius of gyration close to 16 nm. The radius of gyration is expected to follow $R_g = \sqrt{\frac{3}{5}}\, R_{HS}$ and, therefore, to be smaller than the radius we extracted from form factor fits. With a R_g of 16 nm we see a small deviation of 2 nm from the expected value. This is attributed to the selected q-range where the Guinier analysis was performed due to limitation in the experimentally accessible lowest *q*. Regarding I_0, we obtained slightly higher intensities from the linear fits applied on the Guinier plot of the experimental data. This is due to the scattering intensity in the low *q*-regime is not only related to the scattering of the core. Here, the form factor oscillations of the shell are interfering with the scattering signal of the core in the selected *q*-regime. Thus, the measured intensities are influenced by the scattering of the shell and therefore lead to higher scattering intensities at infinitesimal low *q*.

Since we now know the forward scattering intensity, I_0, we can combine this with the Avogadro's number N_A, the density of the silica cores ρ (2.08 g/cm^3), the mass of a single scattering object, *m* (5.08 10^{-17} g) based on the radius of the scattering object and the density of the respective material, the molecular weight, of the scattering object, M_w (3.06 10^7 g/mol) based on the mass of the scattering object, and the difference in scattering length density between the solvent and the scattering object *ΔSLD* to calculate the number concentration *N* according to **equation S25:**

$$N = \frac{I_0\, N_A\, \rho^2}{m\, M_w\, \Delta SLD^2} \qquad \text{(S25)}$$

The extracted number concentrations, as well as the average number concentration $\bar{\bar{N}}$ and the respective standard deviation *SD* are listed in **table S8**.

Table S8. Number concentrations extracted from the scattering intensity of CS microgels dispersions (10wt%)

	I	II	III	IV	$\bar{N}$	*SD*
N (*I*(*q*)) [10^{13} 1/mL]	5.31	5.58	5.81	5.31	5.50	0.21
N (*P*(*q*)) [10^{13} 1/mL]	4.95	5.15	5.64	5.36	5.27	0.26

The average number concentration is 5.5 ± 0.2 10^{12} 1/mL and is, within the experimental errors, virtually the same as the number concentration extracted from the

form factor fits with 5.3 ± 0.3 10^{12} 1/mL. We ascribe the difference between the two values due to the contributions of the polymer shell on the *P(q)* and, therefore, we will use the number concentration extracted from the form factor fits for further calculations.

From the number concentration and the hydrodynamic radius R_h of the CS microgels we can calculate the generalized volume fraction ξ:

$$\xi = N\frac{4}{3}\pi {R_h}^3(T) \quad \text{(S26)}$$

Due to the PNIPAM shell, the hydrodynamic radius and the generalized volume fraction of the CS microgels depend on the temperature as shown in **Figure S15**.

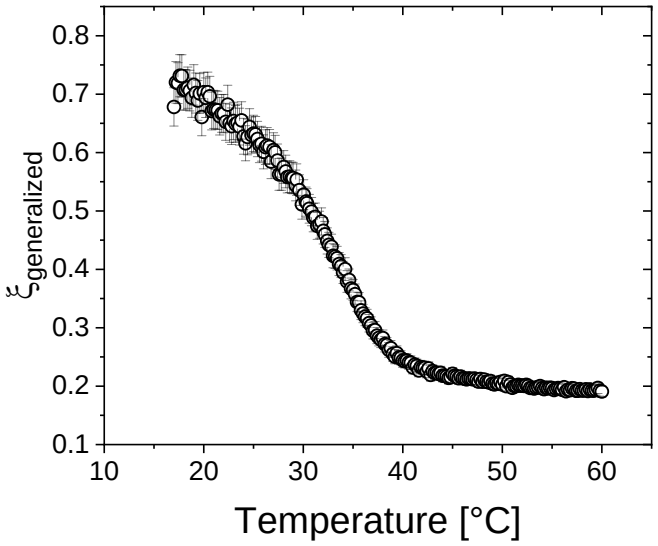

Figure S15. Generalized volume fraction as function of the temperature on the example of a 10 wt% CS microgels dispersion.

The hydrodynamic radius, measured via temperature dependent DLS, directly corresponds to the relation of the generalized volume fraction and the temperature.

Structure factor extraction in the fluid regime

Absorbance spectroscopy has revealed that all CS microgel dispersions (5.4 – 12 wt%) are not in a crystalline state at 40 °C. Thus, we assume that the sample possess a fluid-like structure. To verify this, we conducted SAXS measurements at 40 °C. The 2D detector images of all concentrated samples are shown in **Figure S16**. All scattering patterns exhibiting a fluid-like structure factor contribution as well as intensity

minima related to the form factor of the collapsed CS microgels. No Bragg peaks were observed so the dispersions are in a purely unordered phase.

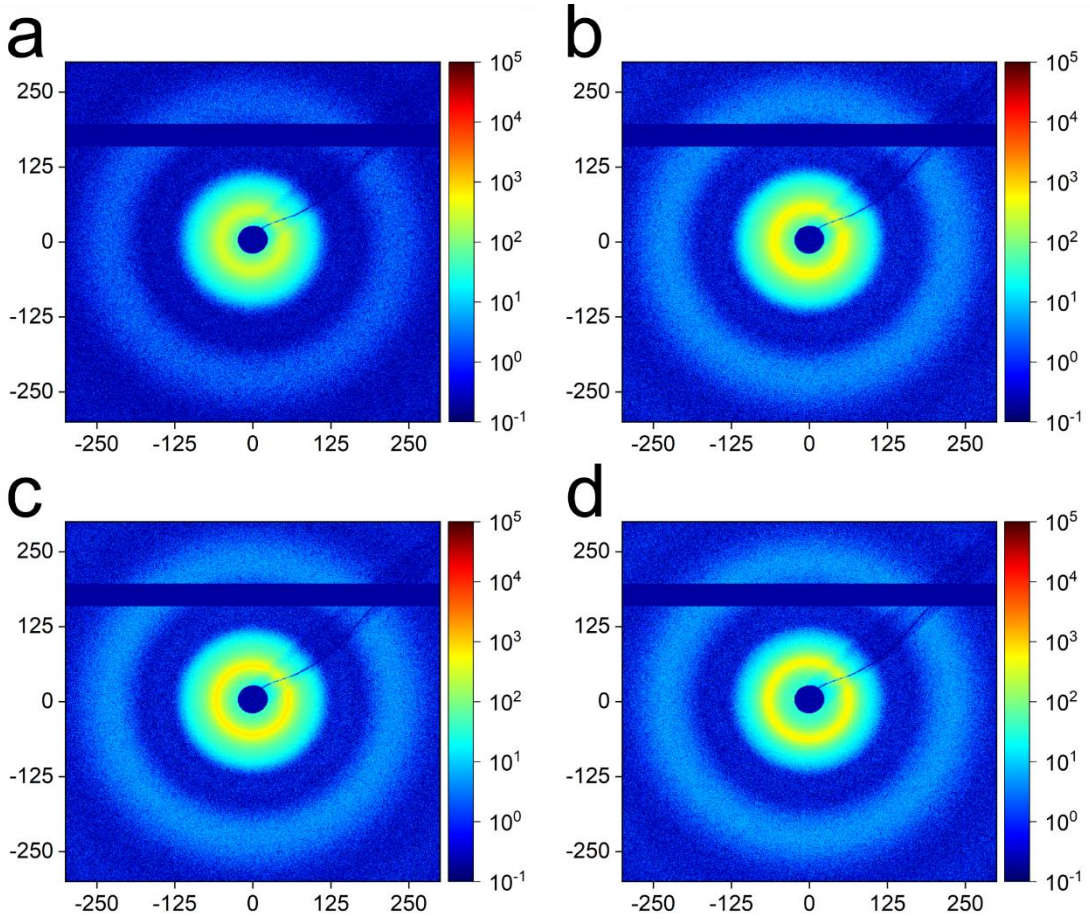

Figure S16. 2D detector images of CS microgel dispersions with mass contents of 5.4, 7.3, 9.1 and 12 wt%.

Radially averaged scattering profiles of the CS microgels with mass contents between 5.4 and 12 wt% recorded at 40 °C are shown in **Figure S17**. While the form factor at mid to high *q* remains unchanged for increasing concentration, the first structure factor maximum in the low *q* region shifts towards higher *q* as indicated by the grey arrow.

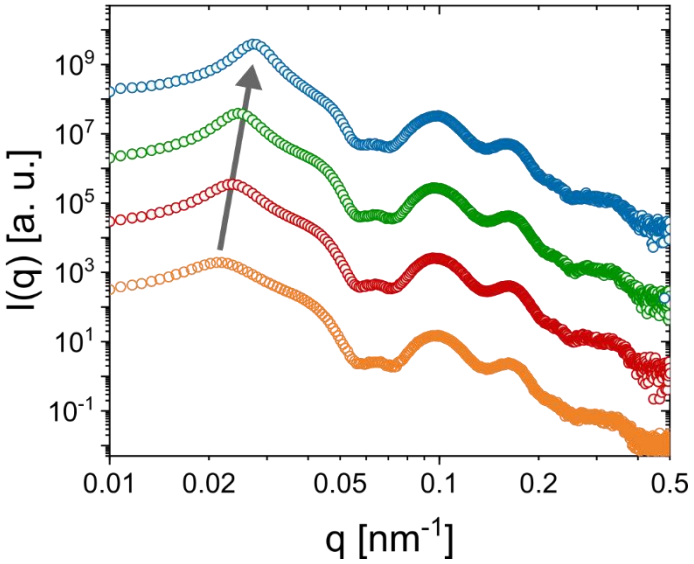

Figure S17. Scattering profiles of samples with 5.4 wt% (orange circles), 7.3 wt% (red circles), 9.1 wt% (green circles) and 12 wt% (blue circles, H_2O) recorded at 40 °C. The grey arrow indicates the shift of the structure factor maximum towards higher *q* with an increase in mass content.

We also measured a sample at a much lower concentration (1.25 wt%) at 40 °C, i.e. at conditions where the microgel shell is collapsed. To our surprise the scattering pattern shown in **Figure S18** exhibits a weak structure factor maximum at $q \approx 0.02$ nm despite the low concentration. Due to this, we did not use the complete scattering profile for the extraction of the structure factor from scattering profiles recorded of the dense samples. The structure factor contribution can be described by the Percus-Yevick hard sphere structure factor model resulting in a volume fraction of 0.16 and a hard sphere radius of 176 nm.

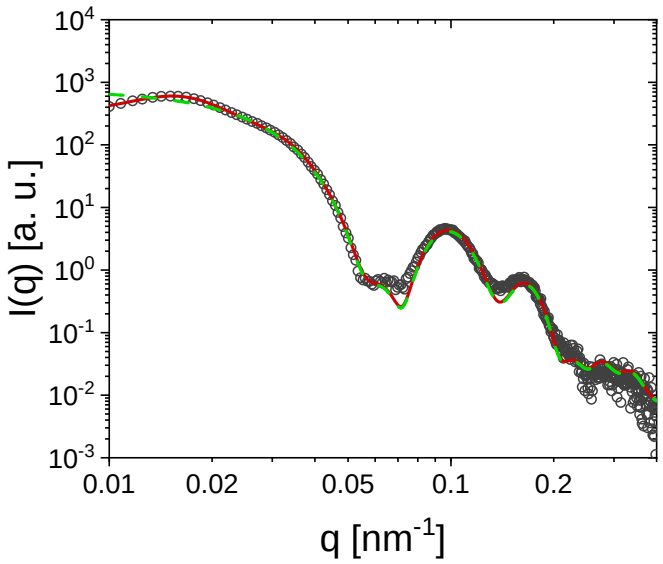

Figure S18. Scattering profile (black circles) recorded from a 1.25 wt% CS microgel dispersion at 40°C. The solid red line corresponds to a combination of form and structure factor fit including a core-homogeneous-shell model and the Percus-Yevick model, respectively. The green dashed line represents a form factor fit without any structure factor.

The structure factor can be calculated from the scattering profiles of the concentrated samples $I_{conc}(q)$ using the known form factor $P(q)_{dilute}$ determined from the dilute sample:

$$S(q) = \frac{I_{\mathrm{conc}}(q)}{scale \cdot P(q)_{\mathrm{dilute}}} \tag{S27}$$

Here *scale* is a scaling factor used to account for the number concentration, scattering contrast as well as the volume of the scattering object (see **eq. S2**). Due to small deviations of the form factor fit and the oscillations of the scattering profile, the extracted structure factors show distinct deviation from unity in the mid to high range of q. Here, the deviations are present even for $q > 0.05$ nm^{-1} where we expect only low amplitudes of the oscillations related to the structure factor. In order to conduct a more realistic structure factor extraction, we used the form factor fit for the extraction in the low q regime ($q < 0.025$ nm^{-1}) which is shown as green dashed line in **Figure S18** and the scattering profile of the dilute CS microgel dispersion for the mid and high q-regime ($q > 0.025$ nm^{-1}) as indicated in **Figure S19b**.

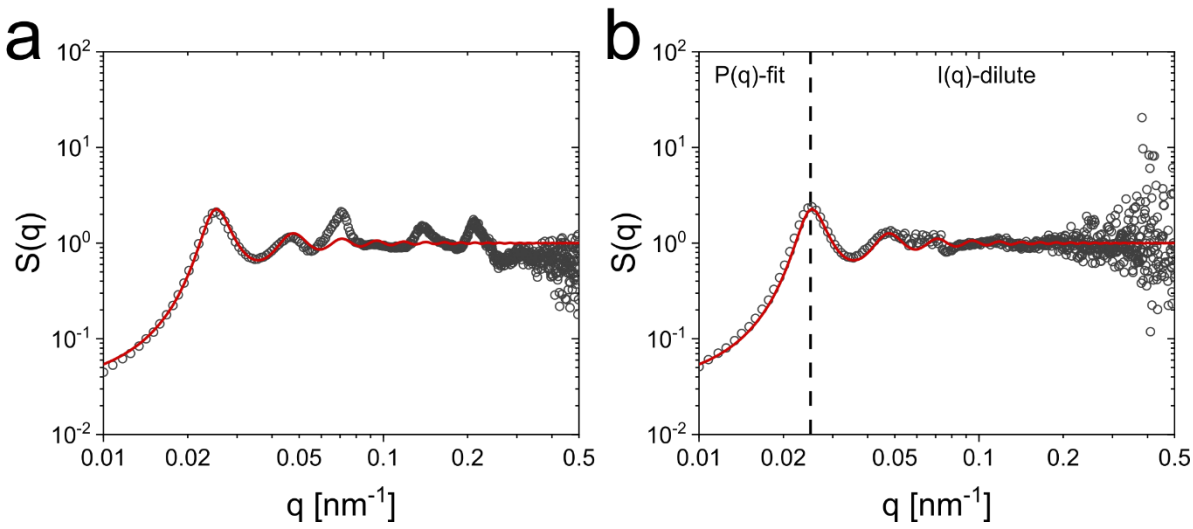

Figure S19. Extracted structure factors from a 9.1 wt% CS microgel dispersion recorded at 40 °C. (a) Extraction based on the form factor fit obtained from fitting the scattering profile of the dilute CS microgel dispersion. (b) Extraction based on the form factor fit for q < 0.025 nm^{-1} and the scattering profile of the CS microgel in the dilute state for q > 0.025 nm^{-1}. The red lines show the structure factor fit (Percus-Yevick).

We fitted the extracted structure factors with the Percus-Yevick hard sphere model. The resulting volume fractions and hard sphere radii are listed in **Table S9**.

Table S9. Parameters obtained from structure factor fits applied to the scattering profiles recorded from CS microgel dispersions at 40°C.

	5.4 wt%	**7.3 wt%**	**9.1 wt%**	**12 wt%**
R_{HS} [nm]	142 ± 11	135 ± 6	133 ± 5	124 ± 4
ϕ_{HS}	0.32 ± 0.08	0.38 ± 0.06	0.43 ± 0.05	0.46 ± 0.04
$S(q)_{q=0}$	0.08	0.05	0.03	0.023

Figure S20 shows the extracted structure factors along with the PY structure factor fits in the regime of low q where deviations between fit and data are expected for soft particles. In our case, fits and data match also in the low q regime indicating that our collapsed CS microgels effectively interact like hard spheres.

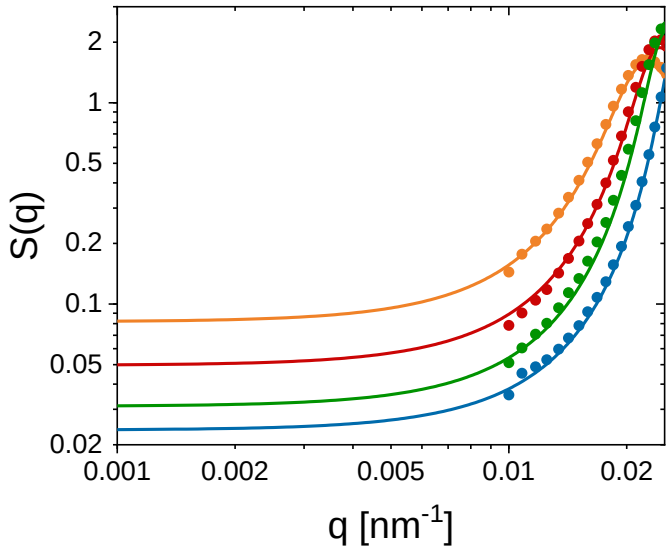

Figure S20. Low *q* region of experimentally determined structure factors (symbols) and Percus-Yevick fits (solid lines) from SAXS measurements of 5.4 wt% (orange dots), 7.3 wt% (red dots), 9.1 wt% (green dots) and 12 wt% (blue dots) samples at 40 °C.

SAXS patterns and simulations for CS microgels in the solid (crystalline) state

The recorded 2D detector images of samples with 5.4, 7.3, 9.1 and 10.9 wt% measured at 20 °C (swollen state) are presented in **Figure S21**. For the 5.4 wt% sample, at the first glance, we see an isotropic scattering pattern in **Figure S21a**, indicating a fluid-like structure. At a closer look, diffraction peaks are visible close to the beamstop, i.e. at low *q*. The large number of peaks and their rather random azimuthal distribution points to a multicrystalline character of the sample. This indicates that this sample is in the fluid-crystalline coexistence region with small, randomly oriented crystallites. Due to the dominant presence of a fluid-like structure factor contribution we consider the 5.4 wt% sample primarily as a fluid, which is in agreement to our findings from absorbance spectroscopy (see main manuscript). For the 7.3, 9.1 and 10.9 wt% samples, we see pronounced sharp Bragg peaks of multiple diffraction orders in **Figure S21b-d**. The hexagonal symmetry of these diffraction patterns indicates close packed structures. The large number of diffraction orders indicates long range order and thus large crystalline domains.

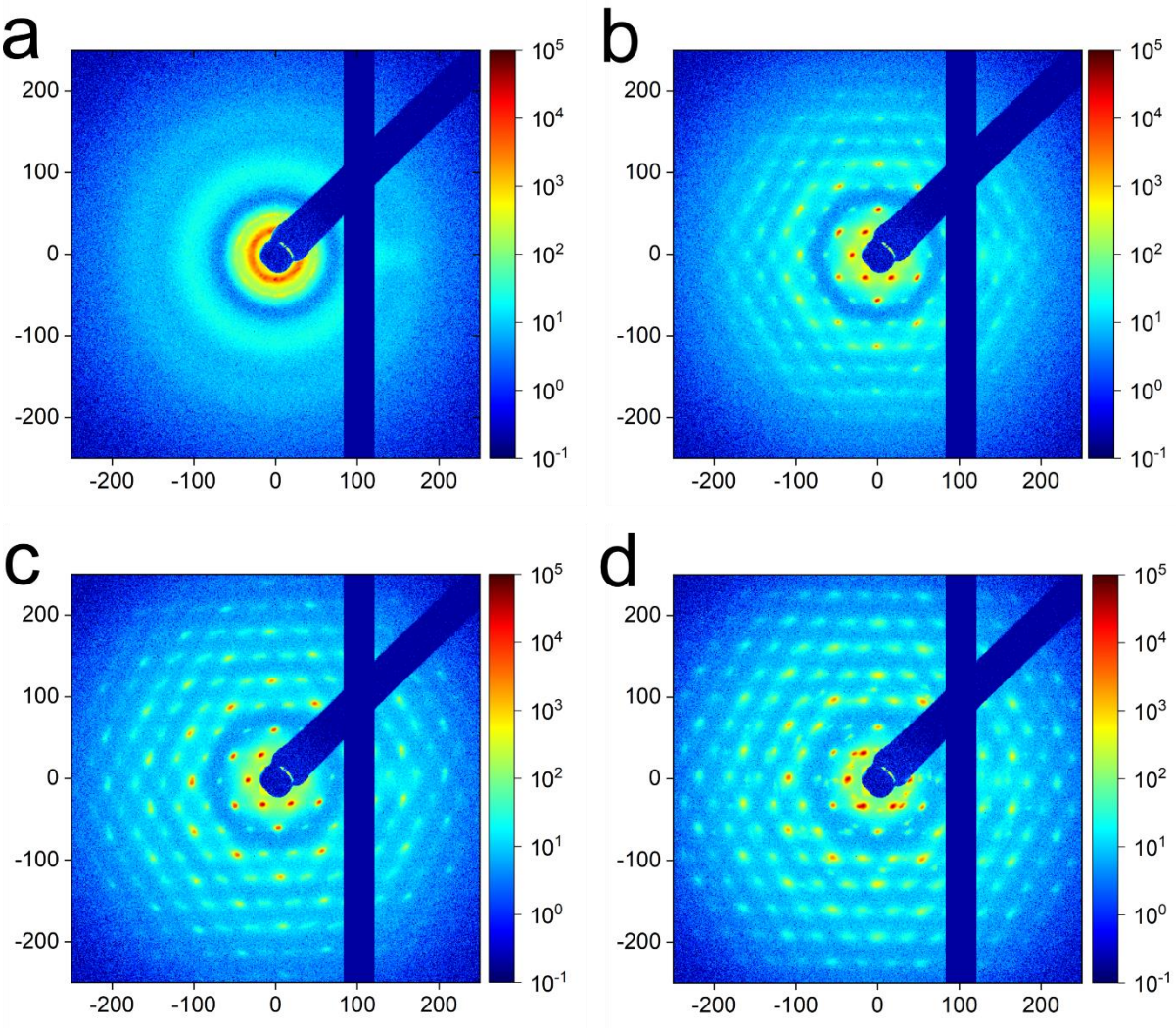

Figure S21. 2D detector images of samples with 5.4 wt% (a), 7.3 wt% (b), 9.1 wt% (c) and 10.9 wt% (d) CS microgels, recorded at a temperature of 20 °C.

In order to identify the crystal structure, we simulated scattering patterns using the software *scatter*.[14] We see an excellent agreement between the recorded (left half) and the simulated pattern (right half) for an hcp structure in **Figure S22**.

The simulations were performed with the 002 plane of the hcp crystal positioned orthogonal to the incident beam. The parameters used in simulations are listed in **Table S10**. We took into account a small particle displacement of 5 nm within the lattices. In **Table S10**, "max. hkl" refers to the orders of Bragg peaks attempted to simulate and ρ refers to the ratio in scattering length density between the polymer shell and the core ($\rho = SLD_{shell} / SLD_{core}$). For simplicity, we used a core-shell model with a homogeneous shell to describe the form factor of the CS microgels. Differences in R_{SAXS} used in this simulation and R_{SAXS} obtained from the form factor analysis are ascribed to the different models used to describe the form factor of the CS microgels.

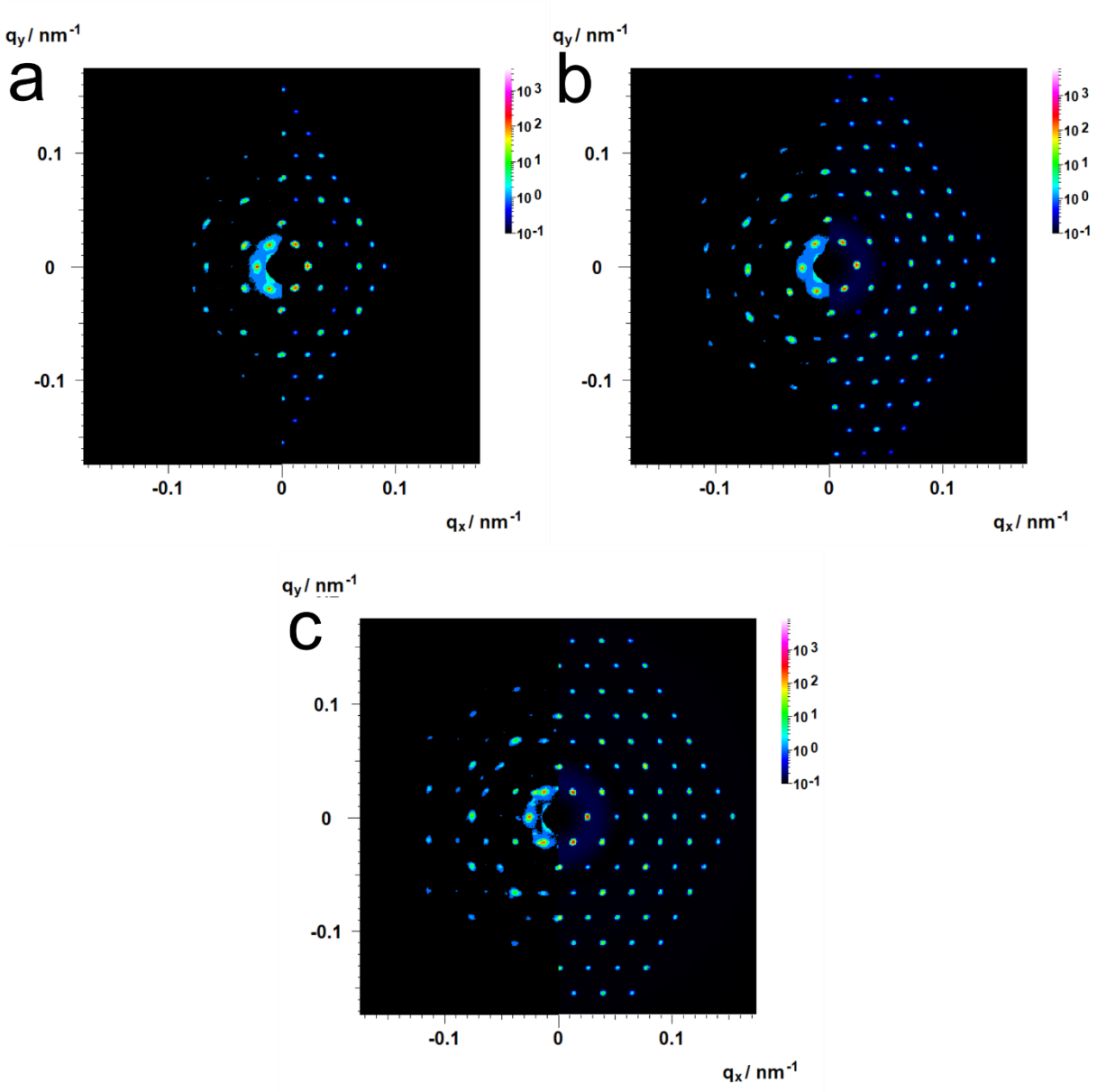

Figure S22. Experimental (left half) and simulated (right half) scattering patterns of samples with 7.3 wt% (a), 9.1 wt% (b) and 10.9 wt% (c) CS microgels. Simulations were performed using a hcp crystal structure with the beam direction orthogonal to the 002 plane.

Table S10. Parameters used to simulate the scattering pattern with a hcp crystal structure.

	7.3 wt%	**9.1 wt%**	**10.9 wt%**
unit cell [nm]	322	303	284
radial domain size [nm]	2700	3000	3200
azimuthal domain size[nm]	2000	2200	2500
displacement [nm]	5	5	5
max. hkl	4	6	6
R_{core} [nm]	18	18	18

σ_{core}	0.1	0.1	0.1
R_{SAXS} [nm]	121	114	104
ρ	0.04	0.04	0.04

Comparison of peak positions for close packed crystal structures

We now want to compare our detected Bragg peaks with the theoretically allowed ones including other crystal structures than hcp. For this, we use the extracted structure factors from the 9.1 wt% sample as an example. The structure factors were extracted by dividing the measured scattering intensity of the dense sample by the form factor contribution of the silica cores (green circles) as well as the form factor of the total CS microgel (blue circles). We plotted all possible peaks corresponding to a hcp structure as vertical lines in the normalized scattering profiles in **Figure S23a**. The profiles were normalized to the position of the first structure factor maximum. The red lines correspond to the Bragg peaks that we could detect in our measured profiles while the grey lines indicate the position of additional, theoretically allowed, peaks. Here, we note that the first structure factor maximum is attributed to the 100 peak, as in the given crystal orientation, the presence of peaks related to 002 and 101 planes is not expected. The peak position is not influenced by the protocol used for the extraction of the structure factor. This is clearly shown as the peak maxima of all three datasets are located on the same positions in *q.*

Since the fcc and hcp crystal structure are energetically very similar and both structures were reported for dense phases of soft microgels, it is worth to compare these to the measured scattering profiles. In **Figure S23b**, the redlines indicate the theoretical position of peaks related to an hcp, the **grey** lines for fcc, and the green lines for peaks shared by both crystal structures. The grey lines do not match with the positions of the recorded Bragg peaks and even for peak positions shared between fcc and hcp structures (green) we only see a match between experimental peaks and theoretical positions at q/q^* = 1.73 and 3. For a rhcp structure, we would expect to detect at least some Bragg peaks solely attributed to an fcc structure. Thus, we can exclude a fcc structure and find no indications for the presence of a rhcp structure. To highlight this ruther we show a selected region of the profiles in the low q/q^* range in **Figure S23c**. In addition, **Figure S23d** highlights only the observed peaks with vertical lines for the hcp structure (red) and the shared peaks between both fcc and hcp structures (green).

Here we want to note that the *q*/*q** normalization regarding the fcc peak positions needed to be performed on the Bragg peak related to the (220) plane. Due to the structural similarities between the hcp and the fcc structure, the crystal plane, referred to as 220 regarding fcc is similar to the 110 plane in hcp, expressing a diffraction peak at the same position. Therefore, these peaks are very convenient for a normalization of the *q*-range, towards comparison of fcc and hcp peaks.

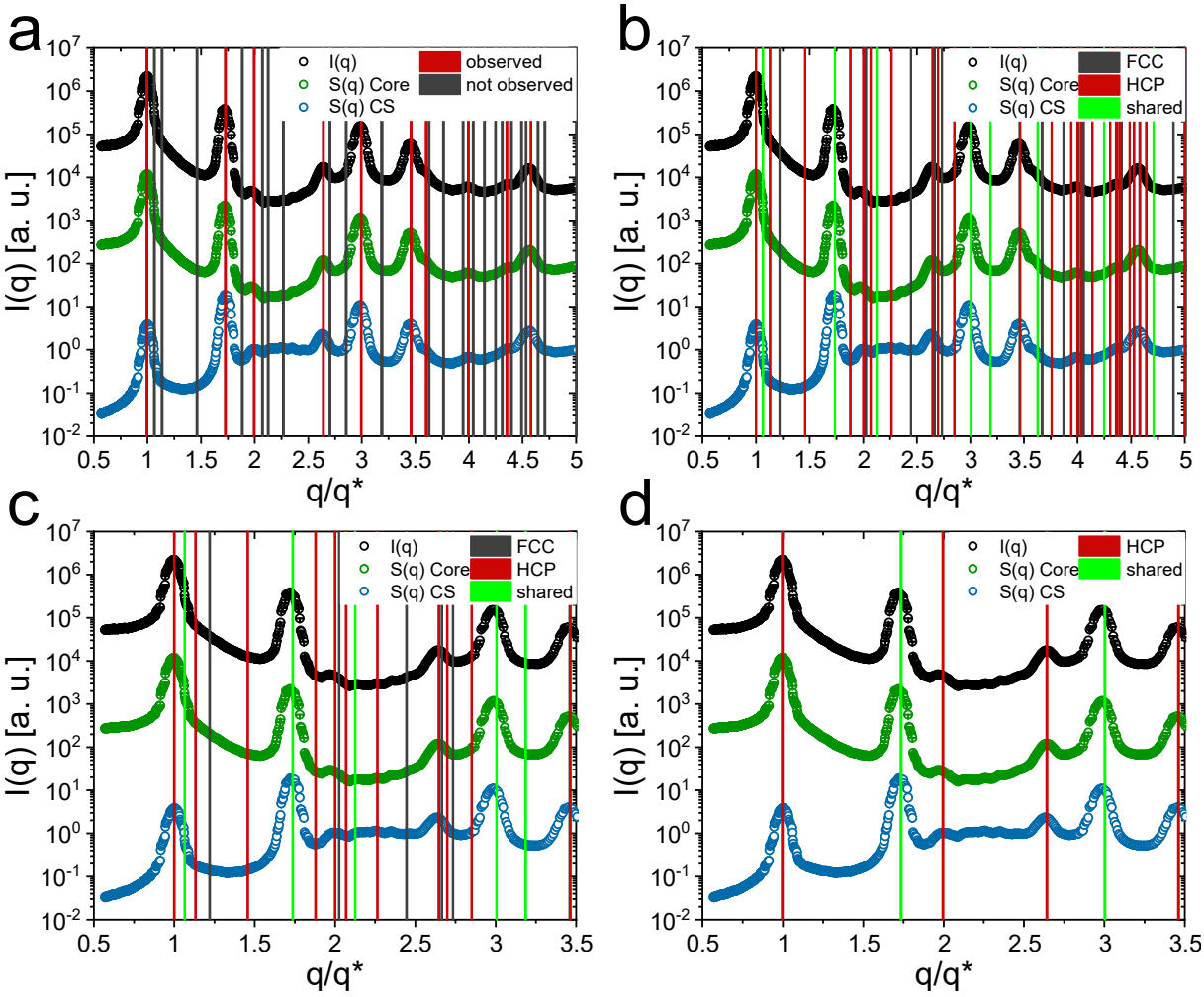

Figure S23. Scattering profiles (black circles) and the extracted structure factors using the form factor of just the core (green circles) and of the total CS microgel (blue circles). (a) The vertical lines correspond to the theoretically allowed peak positions for an hcp crystal structure. Red lines are related to the experimentally observed peaks while the grey lines indicate the position of additional theoretically allowed peaks. (b) Red lines correspond to peak positions of an hcp structure, grey lines are related to an fcc structure and the green lines indicate peaks shared in position between both close packed structures. (c) Same as (b) but with a smaller *q*/*q** range focusing on the low q region. (d) Same as (c) but with a focus on the observed peak positions only, for hcp (red) and the shared peaks with the fcc structure (green).

CS microgel dispersion close to the freezing volume fraction

The 5.4 wt% CS microgel sample exhibits a distinct fluid-like structure factor, but also a Bragg peak around $q \approx 0.03$ nm^{-1} indicating the coexistence with crystallites. In addition to the modeled form factor, we applied a structure factor fit to describe the fluid-like contribution (Percus-Yevick, $S_{\text{fluid}}(q)$) .[15] Here, we want to note that we applied a decoupling approximation instead of a local monodisperse approximation regarding the calculation of the structure factor.[16] Thus, we take into account the polydispersity of our system. The analysis yields a hard sphere radius of 158 nm and a volume fraction ϕ of 0.44. In **Figure S24** we see a good agreement between the fit (black line) and the scattering profile (orange circles). We attribute the deviation between R_{SAXS} and the hard sphere radius to the fuzziness of the microgel shell and potential electrostatic interaction between the CS microgels. The structure factor related to the presence of small crystalline residuals ($S_{\text{crystal}}(q)$) was extracted according to:

$$S_{\text{crystal}}(q) = \frac{I(q)}{N(\Delta SLD)^2 {V_{\text{p}}}^2 P(q) S(q)_{\text{fluid}}} \tag{S28}$$

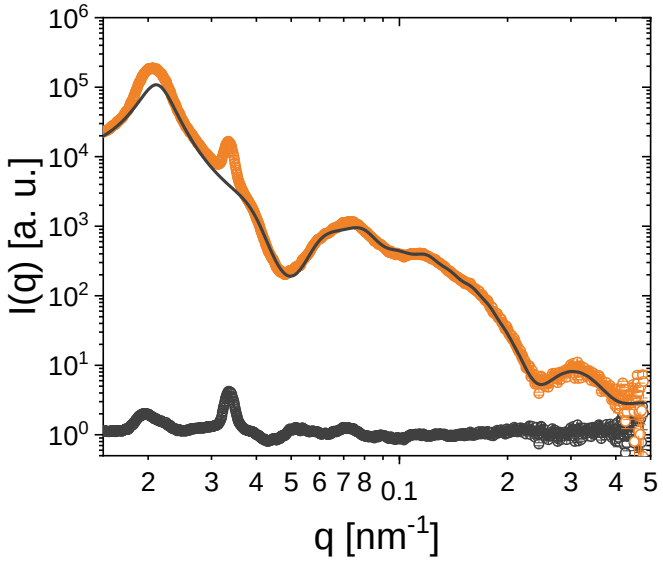

Figure S24. Scattering profile of the 5.4 wt% CS microgel dispersion (orange circles), the respective fit composed of the modeled form factor and the hard sphere structure factor (black line) and the residual structure factor associated to crystalline structures.

The extracted structure factor $S_{\text{crystal}}(q)$, related to the small crystallites only exhibits two Bragg peaks which in this case does not allow for a precise crystal structure

analysis. Based on the CS microgel dispersions possessing higher mass contents we suppose closed packed structures like hcp or fcc.

Lattice compression

From the linear relationship between q_{hkl}, the position of the Bragg peak and the d-spacing of the crystal lattices we can extract the lattice constants a from the slope of the linear fit. From this we can calculate the lattice constant a. The slopes and respective lattice constants are listed in **Table S11**.

Table S11. Slopes and respective lattice constants extracted from linear fits of the Bragg peak position as function of the lattice spacing.

	5.4 wt%	7.3 wt%	9.1 wt%	10.9 wt%
Slope [nm^{-1}]	0.0168	0.0190	0.0205	0.0219
a [nm]	374	331	306	287

We compare the lattice obtained from 2D simulations of the SAXS patterns and the linear relationship between the Bragg peak positions and q_{hkl} in **Figure S25**. In addition, we also added the lattice constants calculated based on the Bragg peaks obtained from Vis-NIR absorbance spectroscopy. All extracted lattice constants are in good agreement with each other.

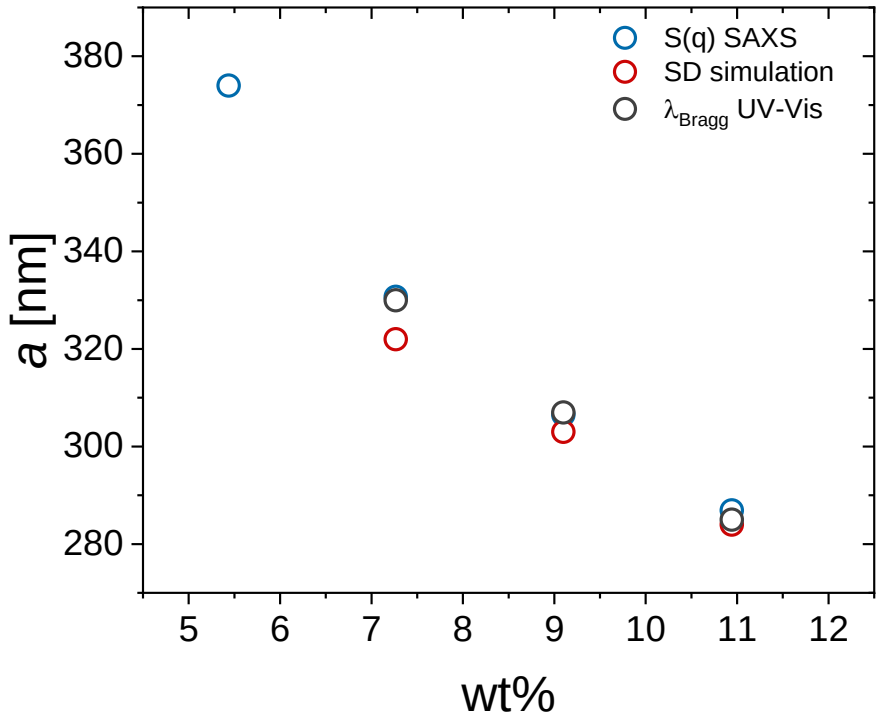

Figure S25. Lattice constants based on the hcp crystal structure extracted from *S*(*q*), 2D simulation of the diffraction pattern and the Bragg peak from Vis-NIR absorbance measurements.

Volume fraction of CS microgels in the colloidal crystals

In addition to the volume fractions calculated based on R_h as well as R_{SAXS} normalized to R_h, we also calculated the volume fraction based solely on R_{SAXS}. Based on the scattering intensity of the SiO_2 cores we obtained the relation between particle number density and the mass content of the CS microgels. With the radius $R_{SAXS,\ dil.}$ of the CS microgels we calculated the generalized volume fraction illustrated as black line in **Figure S26**. In addition, we calculated the volume fraction $\phi_{crystal}$ of the CS microgels based on the lattice constant *a* and $R_{SAXS,\ dil.}$ to compare $\xi_{generalized}$ and $\phi_{crystal}$ according to **equation S22**. We see a good agreement between $\xi_{generalized}$ and $\phi_{crystal}$ which shows the high reliability of the SAXS measurements conducted to extract particle number concentrations. When we include the isotropic osmotic deswelling of the CS microgels at dense packings we see a distinct deviation between the respective volume fractions and $\xi_{generalized}$ for mass contents above 7.3 wt%. The effective volume fractions of the CS microgels seems to stay constant around 0.43 where we identified the solid phases.

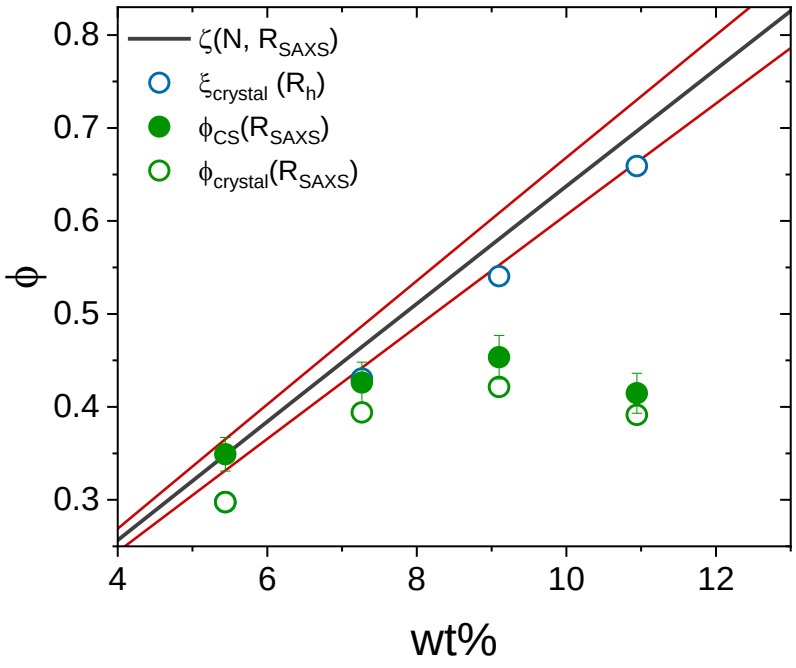

Figure S26. Relation between volume fraction and mass content of the CS microgels. The solid black line is related to the generalized volume fraction extracted from particle number concentration and $R_{SAXS,\ dil.}$ obtained from the P(q) of the dilute CS microgel dispersion. The red lines indicate the respective standard deviation. Green and blue circles are related to the volume fraction of the CS microgels based on the unit cell dimensions. For the blue circles the CS microgel volume is based on R_{SAXS} from dilute dispersion, while for the green circles R_{SAXS} is obtained from the respective modeled form factor in dense packing. The green dots indicate the volume fraction of the CS microgels based on the particle number concentration and the radius extracted from the respective modeled form factor in dense packing.

Williamson-Hall analysis

We performed a Williamson-Hall analysis to extract the radial and azimuthal sizes of the coherently scattering domains.[17] **Figure S27** shows the square of the FWHM of the Bragg peaks $w_{rad/azi}$ as function of the position of the Bragg peak in q^2. The FWHM and peak positions, regarding the radial domain sizes were extracted by the application of a Gaussian-fit-function on the Bragg peaks in the structure factor profiles. While for the determination of the azimuthal domain size we performed automated image analysis to apply gaussian fits on the azimuthal profiles of the respective Bragg peaks. A linear fit was applied on the obtained data according to:

$$w_{\mathrm{rad/azi}}{}^2(q) = \left(\frac{2\pi}{L_{\mathrm{rad/azi}}}\right)^2 + g_{\mathrm{rad/azi}}\, q^2 \qquad \text{(S29)}$$

Here $L_{rad/azi}$ is related to the size of coherently scattering domains and $g_{rad/azi}$ is related to strains of the crystallites. $L_{rad/azi}$ can be extracted from the intercept of the linear fit and is presented in **Figure 27**. The extraction of $g_{rad/azi}$ leads to strains below 1% which is reflected by the small slope of the linear fits. From this we conclude that we have domain sizes of 3 to 4 µm with nearly no strains present for our colloidal crystals based on CS microgels.

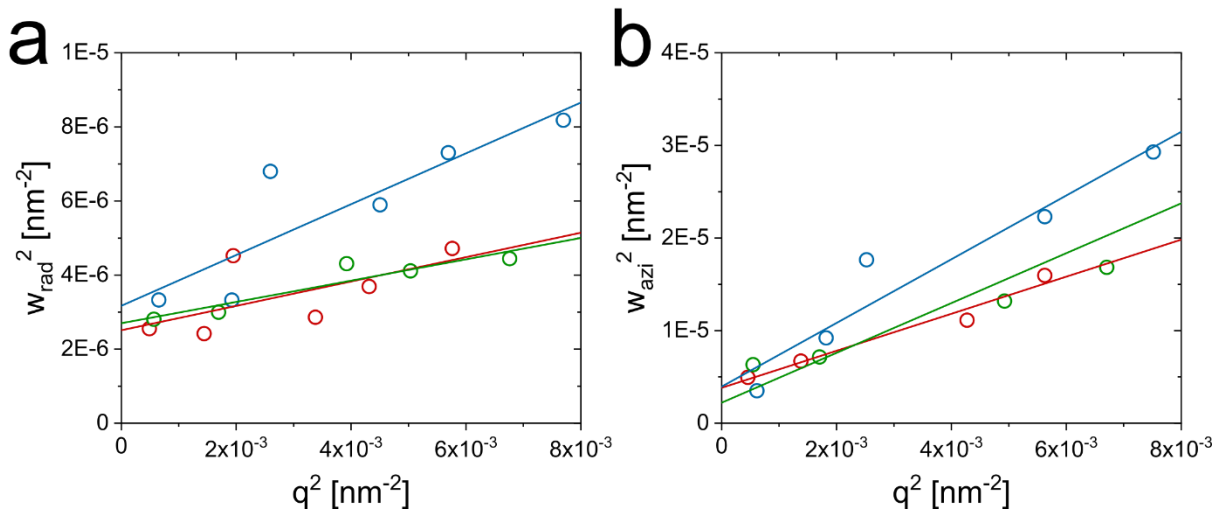

Figure S27. Williamson-Hall analysis applied on the Bragg peaks to extract the size of the coherently scattering domains of the colloidal crystals in (a) radial and (b) azimuthal sizes. Square of the FWHM from the Bragg peaks obtained from a gaussian fit as function of q^2. Data obtained from CS microgel dispersion with mass contents of 7.3 wt% is shown in red, green is related to 9.1 wt% and blue to 10.9 wt%. The solid lines correspond to linear fits to the data.

Form factor modeling and radial density profiles of CS microgels at dense packing

The distinct form factor oscillations in the scattering profiles of the CS microgel dispersions with high mass contents from 5.4 to 10.9 wt% enabled a detailed form factor analysis, based on the same core-exponential-shell model which was used to fit the scattering profile of the CS microgels in the dilute state. The parameters applied for the form factor modeling are listed in **Table S12**.

Table S12. Parameters used for the form factor modeling (**eq. S3** and **S4**) of the CS microgel dispersions in the concentrated regime.

Parameters	5.4 wt%	7.3 wt%	9.1 wt%	10.9 wt%
scale	0.28	0.34	0.36	0.39
IB [a. u.]	0.2	0.2	0.2	0.2
R_{core} [nm]	18	18	18	18
Δt_{shell} [nm]	120	116	109	98
SLD_{core} [10^{-6} Å^{-2}]	17.75	17.75	17.75	17.75
$SLD_{shell,\ in}$ [10^{-6} Å^{-2}]	9.89	9.89	9.89	9.89
$SLD_{shell,\ out}$ [10^{-6} Å^{-2}]	9.43	9.43	9.43	9.43
$SLD_{solvent}$ [10^{-6} Å^{-2}]	9.43	9.43	9.43	9.43
σ_{core}	0.1	0.1	0.1	0.1
σ_{shell}	0.08	0.08	0.08	0.08
A	2.2	2.6	3.5	4.9

In addition, we were able to extract the radial density profiles of the CS microgels from the modeled form factor shown in **Figure S28a**. The density profile exhibits high *ΔSLD* values until reaching a radius of 18 nm, representing the SiO_2 core. From this point we see an exponential decrease in contrast *ΔSLD* which is related to the inhomogeneous structure of the microgel shell. With an increase in concentration the decline of the shell contrast gets more and more pronounced, also resulting in a decrease of the thickness of the shell. We integrated the regime of the density profile associated with the microgel shell for all profiles, presented in **Figure 28b**, in order to ensure constant mass and the validity of the *ΔSLD* profiles. Here we want to note that the *SLD*s of SiO_2 and the PNIPAM microgel shell were obtained from the *SLD* calculator provided by NIST.[18]

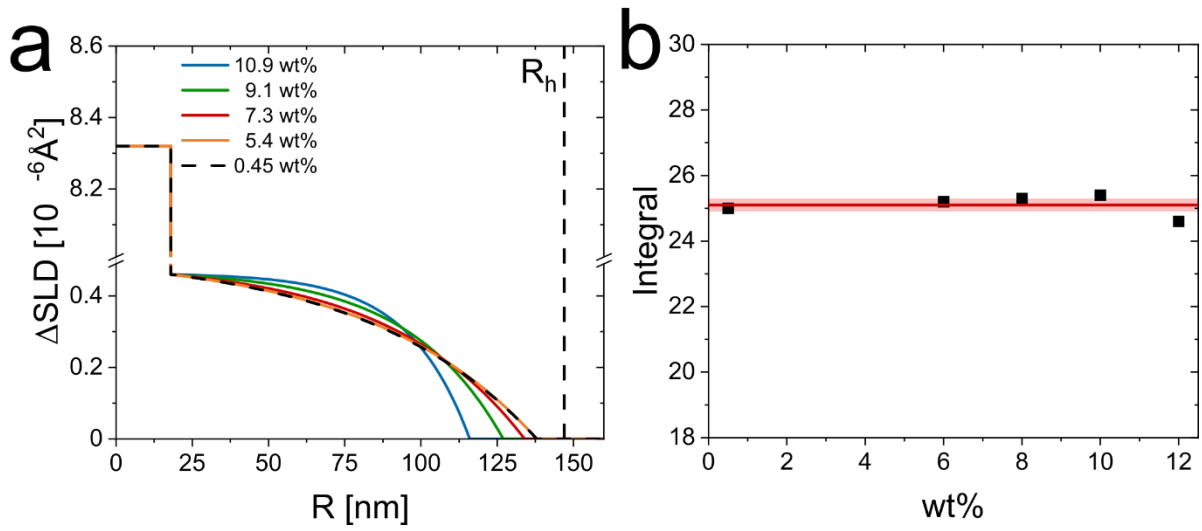

Figure S28. (a) Radial *ΔSLD* profiles extracted from the modeled and fitted form factors of the CS microgels in dense packings and dilute state based on the core-shell model, exhibiting an exponential decay in the *SLD* profile of the shell (**eq. S3**). For the sake of clarity, we added a break on the y-axis, due to the strong differences in *ΔSLD* between the core and the shell. (b) The integrals of the microgel shell extracted from the radial *ΔSLD* profile in dependence of the respective mass content.

References

1 M. Hildebrandt, S. Lazarev, J. Pérez, I. A. Vartanyants, J. M. Meijer and M. Karg, *Macromolecules*, 2022, **55**, 2959-2969.

2 M. Ballauff, *Curr Opin Colloid In*, 2001, **6**, 132-139.

3 J. Polte, T. T. Ahner, F. Delissen, S. Sokolov, F. Emmerling, A. F. Thünemann and R. Kraehnert, *J Am Chem Soc*, 2010, **132**, 1296-1301.

4 SasView, http://www.sasview.org/).

5 L. A. Feigin and D. I. Svergun, *Structure Analysis by Small-Angle X-ray and Neutron Scattering*, Springer New York, NY, 1987.

6 M. Stieger, W. Richtering, J. S. Pedersen and P. Lindner, *The Journal of Chemical Physics*, 2004, **120**, 6197-6206.

7 I. Berndt, J. S. Pedersen, P. Lindner and W. Richtering, *Langmuir*, 2006, **22**, 459-468.

8 I. Bressler, J. Kohlbrecher and A. F. Thünemann, *J Appl Crystallogr*, 2015, **48**, 1587-1598.

9 E. Ponomareva, B. Tadgell, M. Hildebrandt, M. Krüsmann, S. Prévost, P. Mulvaney and M. Karg, *Soft Matter*, 2022, **18**, 807-825.

10 S. W. Provencher, *Comput Phys Commun*, 1982, **27**, 213-227.

11 J. Schindelin, I. Arganda-Carreras, E. Frise, V. Kaynig, M. Longair, T. Pietzsch, S. Preibisch, C. Rueden, S. Saalfeld, B. Schmid, J. Y. Tinevez, D. J. White, V. Hartenstein, K. Eliceiri, P. Tomancak and A. Cardona, *Nature Methods*, 2012, **9**, 676-682.

12 C. I. Aguirre, E. Reguera and A. Stein, *Advanced Functional Materials*, 2010, **20**, 2565-2578.
13 A. Rauh, N. Carl, R. Schweins and M. Karg, *Langmuir*, 2018, **34**, 854-867.
14 S. Förster, L. Apostol and W. Bras, *J Appl Crystallogr*, 2010, **43**, 639-646.
15 J. K. Percus and G. J. Yevick, *Phys Rev*, 1958, **110**, 1-13.
16 M. Kotlarchyk and S. H. Chen, *Journal of Chemical Physics*, 1983, **79**, 2461-2469.
17 E. A. Sulyanova, A. Shabalin, A. V. Zozulya, J. M. Meijer, D. Dzhigaev, O. Gorobtsov, R. P. Kurta, S. Lazarev, U. Lorenz, A. Singer, O. Yefanov, I. Zaluzhnyy, I. Besedin, M. Sprung, A. V. Petukhov and I. A. Vartanyants, *Langmuir*, 2015, **31**, 5274-5283.
18 NCNR, https://www.ncnr.nist.gov/resources/activation/, (accessed 2022-17-03).